Chapter 4

T_2 Relaxation and Diffusion Measurements of Hyperpolarized ^{129}Xe and ^{3}He in the Pulsed Low-Field Resistive MR Scanner

4.1 Background

The transverse relaxation time T_2 characterizes the rate of magnetization decay in the plane perpendicular (or transverse) to the static magnetic field $B_\circ$ after the magnetization has been tipped away from the $B_\circ$ field by an RF pulse. The transverse magnetization decay results as spins lose their coherence while they precess with slightly different Larmor frequencies in the transverse plane. The dispersion in frequencies in turn occurs when the spins precess in different magnetic fields. There are three causes for this field variation [29]. First, the external field is not perfectly homogeneous and therefore varies slightly across the sample. Second, each spin creates a magnetic dipole field that affects the neighboring spins. This is commonly referred to as spin-spin interaction. Depending on the spin density distribution, the fields seen by the spins at different positions can be slightly different. Lastly, if spins move (diffuse) within the sample in the presence of background magnetic gradients[1], they experience a time varying field. The end result of the three scenarios is that some of the spins acquire extra phase, which leads to de-phasing and consequently, loss of MR signal.

In conventional MR, the transverse relaxation rate determines the amount of time available for imaging between each 90-degree RF excitation pulse. In spin echo imaging of water,

---

[1] The background gradients can either be due to field inhomogeneities or due to the externally applied gradients.

for instance, one acquires one or two lines of k-space [59] after each 90-degree RF excitation.[2] Therefore, the T_2 relaxation rate of water presents a limit on the time available for imaging one line of k-space. Once the transverse polarization of water is lost, the longitudinal thermal polarization is allowed to *grow* towards its thermal equilibrium value. A new 90-degree RF pulse flips the magnetization again into the transverse plane so that a new line of k-space is collected.

In contrast, the transverse relaxation rate of hyperpolarized gas determines the *total* time available for imaging in a spin echo sequence due to the nonrenewable nature of gas hyperpolarization. The longitudinal magnetization of hyperpolarized gas *decays* (rather than *grows*) with a time constant T_1 towards its thermal equilibrium. Hence, it does not pay off to wait after the transverse magnetization has decayed; the longitudinal magnetization will not recover to its initial hyper-value. To deal with the problem of nonrenewable polarization, small flip-angle pulse-sequences have primarily been used [6, 68]. However, such pulse sequences make poor use of the available magnetization as each acquisition only uses a small fraction ($\sin\alpha$, where α is the flip-angle) of the available magnetization. Since the inherent transverse relaxation times of gases[3] are an order of magnitude longer than for liquids [59], the entire k-space could be sampled using a single-shot (i.e, single 90-degree pulse) spin echo sequence. Such sequences should give a superior SNR compared to small flip-angle sequences because they use all the available magnetization ($\alpha = 90°$) to encode the image-domain data (see Section 4.6 for more details). In fact, imaging with the entire magnetization vector versus a 12-degree projection of the initial magnetization increases the SNR by a factor of around 5 ($\sin 90°/\sin 12° \approx 5$). This is equivalent to increasing the initial ^{129}Xe hyperpolarization from 5% to 25%–a goal that has proven to be very difficult to achieve.

Our aim was to implement a single-shot spin echo imaging sequence (also called CPMG sequence, after Carr-Purcell-Meiboom-Gill [69, 70], on the pulsed low-field resistive MR scanner. In particular, we wanted to investigate whether the resistive pulsed system was stable enough to maintain the stringent phase stability required during the CPMG condition. Studying T_2^{CPMG} relaxation enabled us to estimate the phase stability of the resistive scanner and to identify other potential problems of using the resistive system for spin echo

---

[2] K-space (or time-domain space) is the Fourier transform of image-domain space.

[3] The inherent transverse relaxation times should be understood as the transverse relaxation times resulting exclusively from spin-spin interactions.

imaging.

Furthermore, by varying the interecho spacing in the CPMG spin echo sequence, we were able to differentiate between the T_2^{CPMG} relaxation times and the inherent T_2 relaxation of gases. The T_2^{CPMG} relaxation characterizes the decay of a spin echo train in a particular magnetic environment and thus includes diffusion losses in the background gradients, while the inherent T_2 relaxation times of gases are purely the property of the gas mixture used. The inherent T_2 times of ^{129}Xe and ^{3}He mixtures used in the hyperpolarized gas experiments are a useful measure of the absolute limit on the imaging time when using a CPMG sequence. To the best of our knowledge, past experiments measuring the transverse relaxation times of ^{129}Xe and ^{3}He [47, 71, 72, 26, 73, 28, 74, 75, 76, 77] did not remove the effects of diffusion losses in the static background (remnant) gradients. The values of T_2 relaxation times quoted in the literature are thus comparable to what we call T_2^{CPMG} relaxation, and not to the inherent T_2 relaxation.

Apart from the non-renewable nature of the noble gas polarization, large diffusion of gases is another factor that makes imaging of hyperpolarized gas difficult, and more importantly, dictates pulse-sequence design. Diffusion of spins through magnetic field gradients causes loss of NMR signal and limits the maximum achievable resolution. The reduced susceptibility effect and smaller magnetic field heterogeneities at low fields should help decrease signal loss due to diffusion in our low-field system. However, in order to predict MR signal loss during imaging with spin echo and/or gradient echo sequences, we had to evaluate the diffusion coefficient of hyperpolarized gases on our system. Diffusion coefficients for ^{129}Xe and ^{3}He *in vitro* have been measured. Patyal *et al.* [78] performed measurements of ^{129}Xe diffusion coefficient while Bock *et al.* [79] and Schmidt *et al.* [80] measured diffusion coefficient of ^{3}He. However, all these measurements were done using low flip-angle techniques (gradient echo, DANTE) which suffer from poor SNR and are limited by T_1 relaxation. Some fast sequences, such as BURST from Wolber *et al.* [81] and Peled *et al.* [82] avoided the problem of T_1 relaxation, but had a complicated spin dynamics. Mair *et al.* [83] and Zhao *et al.* [77] established the advantage of high SNR techniques based on multiple spin echo sequences (RARE, CPMG). These techniques enable the use of multiple diffusive attenuations within a single sequence and thus allow the measurement of time-dependant (or restricted) gas diffusion [83]. However, to remove diffusion losses in the background gradients from the total signal decay, the experiments in [83] and [77] required two shots (i.e., two separate CPMG trains) as well as the normalization of the echo train against the first echo. Two (or multi) shot spin echo sequences are impractical in the case of hyperpolarized gases because of the non-renewable gas polarization.

Our single-shot CPMG sequence for measuring diffusion coefficient uses all the available magnetization and thus has inherently high SNR. In addition, the chosen sequence enabled us to separate T_2^{CPMG} relaxation of the gas from diffusive loses in the external gradients. Finally, by comparing the experimental measurement of ^{3}He, ^{129}Xe and water diffusion coefficients with theoretical estimations, we were able to determine the precision of our single-shot CPMG sequence for measuring diffusion coefficients.

4.2 Theory of Transverse (T2) Relaxation

As mentioned in Section 4.1, the transverse component of magnetization decays due to magnetic fluctuations which cause spreading in the Larmor frequency of the spin ensemble and, consequently, dephasing. The rate of decay of the transverse component M_{xy} is proportional to the instantaneous value of the transverse magnetization,

$$\frac{dM_{xy}}{dt} = -\frac{M_{xy}}{T_2^*}, \tag{4.1}$$

where the transverse relaxation coefficient T_2^* includes the relaxation due to static magnetic field inhomogeneities, $T_{\Delta B_z}$, the inherent relaxation due to spin-spin interactions, T_2, and relaxation due to the diffusion of spins in the magnetic field gradients, T_D.[4] To summarize:

$$\frac{1}{T_2^*} = \frac{1}{T_{\Delta B_z}} + \frac{1}{T_2} + \frac{1}{T_D}. \tag{4.2}$$

Later in the chapter we will show how to separate the $1/T_{\Delta B_z}$ term from the rest of relaxation using spin echoes. Once that is accomplished, we proceed to identify the $1/T_D$ term and distinguish it from the inherent $1/T_2$ relaxation of hyperpolarized gases (^{129}Xe ad ^{3}He).

The solution to Eq. 4.1, after a 90-degree excitation ($M_{xy}(0) = M_\circ$), is

$$M_{xy} = M_\circ e^{-t/T_2^*}. \tag{4.3}$$

Equation 4.3 describes the macroscopic behavior of the transverse component of the magnetization. However, to understand how the above relationship arises as a result of the microscopic motion of magnetic moments, one has to consider the equations of motion of the individual spins and then average over the spin population.

The magnetic field seen by the jth spin is $\mathbf{B}_j = (B_\circ + b_j)\mathbf{k}$, where $B_\circ\mathbf{k}$ is the static magnetic field pointing in the z-direction and $b_j\mathbf{k}$ is the z component of the field fluctuations seen by the jth spin.[5] For mobile (i.e., diffusing) spins, b_j is time-varying. The equation of

---

[4] It should be pointed out that most books on the subject of MR relaxation define Eq. 4.1 in terms of T_2 and not T_2^* as is done here.

[5] This discussion assumes that only those fluctuations in b_j that are parallel to $B_\circ$ cause variations in Larmor frequency and therefore transverse relaxation. This approximation is invalid when dealing with longitudinal relaxation or non-adiabatic transverse relaxation.

motion for the jth magnetic moment is

$$\dot{\boldsymbol{\mu}}_j = \gamma \boldsymbol{\mu}_j \times \mathbf{B}_j = \gamma \boldsymbol{\mu}_j \times [B_\circ + b_j(t)]\mathbf{k}. \tag{4.4}$$

Combining the x and y transverse components of the magnetic moment into a single complex μ, such that $\mu_j = \mu_{j,x} + \mu_{j,y}$, the equations of motion become

$$\dot{\mu}_j(t) = -i\gamma[B_\circ + b_j(t)]\mu_j(t). \tag{4.5}$$

After integration, the above equation gives

$$\mu_j(t) = \exp\left(-i\gamma B_\circ t\right) \exp\left[-i\gamma \int_0^t b_j(\tau)d\tau\right]\mu_j(0), \tag{4.6}$$

where $\mu_j(0)$ is the initial magnetization of the jth spin. To get the total transverse magnetization, we have to sum over N particles in the system:

$$\begin{aligned} \mathbf{M} &= \frac{1}{V}\sum_{j=1}^{N} \boldsymbol{\mu}_j & (4.7) \\ &= \frac{1}{V}\sum_{j=1}^{N} \exp\left[-i\gamma B_\circ t - i\gamma \int_0^t b_j(\tau)d\tau\right]\mu_j(0). & (4.8) \end{aligned}$$

Since the initial value of the magnetic moment $\mu_j(0)$ is independent of its local field b_j the initial magnetization can be factored out:

$$M(0) = \frac{1}{V}\sum_{j=1}^{N} \mu_j(0). \tag{4.9}$$

By also factoring out the exponential representing the precession around $B_\circ$ field, the complex transverse magnetization is finally given by

$$M(t) = \exp\left(-i\gamma B_\circ t\right) \left\{ \frac{1}{N}\sum_{j=1}^{N} \exp\left[-i\gamma \int_0^t b_j(\tau)d\tau\right] \right\} M(0). \tag{4.10}$$

Equation 4.10 describes the behavior of the transverse magnetization, also called the Free-Induction-Decay (FID). The first term represents the oscillatory part of the FID–the oscillation of magnetization around $B_\circ$, with the characteristic Larmor frequency $\omega_\circ = \gamma B_\circ$, where γ is the gyromagnetic ratio of the spin. The last term is the initial value of magnetization. The term in the curly brackets is the envelope of the FID–the relaxation of the transverse magnetization.

Let us look more closely at the relaxation part of the FID. The time integral over the magnetic fluctuations seen by the jth particle in Eq. 4.10 can be related to the accumulated phase angle $\phi_j(t)$, where

$$\phi_j(t) = -\gamma \int_0^t b(\tau) d\tau. \tag{4.11}$$

The average over the population of particles can then be written as

$$\begin{aligned} F(t) &= \frac{1}{N}\sum_{j=1}^{N} \exp\left[-i\phi(t)\right] = \langle \exp\left[-i\phi(t)\right]\rangle & (4.12)\\ F(t) &= \int P[\phi(t)] \exp\left[i\phi(t)\right] d\phi, & (4.13) \end{aligned}$$

where $P[\phi(t)]d\phi$ is the probability that a spin had accumulated a phase between ϕ and $\phi + d\phi$ in a time t. To solve Eq. 4.13, we have to assume a functional form for the probability function. Since the spin samples many different fields over a short time, we can invoke the Central Limit Theorem [29]. The probability distribution of phase angles can thus be described using a Gaussian function, with zero mean angle and a mean square width of $\langle\phi^2\rangle$:

$$P(\phi) = \frac{1}{(2\pi\langle\phi^2\rangle)^{\frac{1}{2}}} \exp\left(-\frac{\phi^2}{2\langle\phi^2\rangle}\right). \tag{4.14}$$

The relaxation of the FID signal, using a Gaussian distribution for the spin phase angles, is

$$F(t) = \frac{1}{(2\pi\langle\phi^2\rangle)^{\frac{1}{2}}} \int_{-\infty}^{\infty} \exp\left(-\frac{\phi^2}{2\langle\phi^2\rangle}\right) \exp\left(i\phi\right) d\phi. \tag{4.15}$$

The integral above can be evaluated by completing the square of the arguments of the exponentials. The result is

$$F(t) = \exp\left[-\frac{\langle\phi^2(t)\rangle}{2}\right] \equiv \exp\left[-\frac{t}{T_2^*}\right]. \tag{4.16}$$

To make further progress on the equation above would require us to know the mean square width of the phase angles sampled by the spins. Nevertheless, by starting with the equation of motion for the individual spins (Eq. 4.4) and then averaging over the spin population, we were able to show that the transverse magnetization can be expressed as

$$M(t) = M(0)\exp(-i\omega_\circ t)F(t), \tag{4.17}$$

where F(t) is given by Eq. 4.16. We will return to this equation as well as Eq. 4.10 in the following chapters when describing the effects of magnetic field inhomogeneities and the effect of diffusion on transverse relaxation.

4.3 Reversible T2 Decay

Equation 4.2 tells us that part of the transverse relaxation is due to the inhomogeneities in the main magnetic field. Spins at different positions in the sample dephase because they see a different field. Fortunately, the magnetization lost due to dephasing in an inhomogeneous magnet can be recovered using the technique of spin echoes.

4.3.1 Magnet Inhomogeneities and Spin Echoes

The easiest way to understand the occurrence of a spin echo is to draw on the analogy between the spins precessing in an inhomogeneous magnetic field and runners running with different speeds on a track course. Imagine the runners started running at the same time and place on the track. After some time t into the run, the runners will be spread along the course of the run, with the fastest runner furthest away from the start and the slowest one the closest. If at time t, the runners are made to turn back (i.e., reverse direction of running by 180°) and if they continue to run at the same speed, they will all reach the start at the same time, namely, at time $2t$. The distance by which the fastest runner was ahead of the slowest one before time t, he gets behind after time t; what used to be an advantage turned into a disadvantage. Similarly, the spins in a higher magnetic field precess faster than the spins in the lower magnetic field. After a time t, the fast spins will have gained an additional $\Delta\phi$ of phase relative to the slow spins. If the sense of spin precession is reversed at time t (with a 180-degree pulse), then the spins will again have the same phase at time $2t$. In other words, the coherence of spins will be fully restored at time $2t$.

To demonstrate the concept of spin echoes formally, we return to Eq. 4.10, representing the behavior of transverse magnetization at time t, where $b_j(t)$ is the magnetic field variation seen by the jth particle. It is best to transform this equation to the rotating frame of reference. In the rotating frame, the Larmor precession is not detectable. Thus,

$$M(t) = \frac{1}{N}\sum_{j=1}^{N} \exp\left[-i\gamma \int_0^t b_j(\tau)d\tau\right] M(0). \tag{4.18}$$

If a π pulse is applied at time t about an axis in the transverse plane, all spins will be rotated through a 180-degree angle and the net complex magnetization vector M will

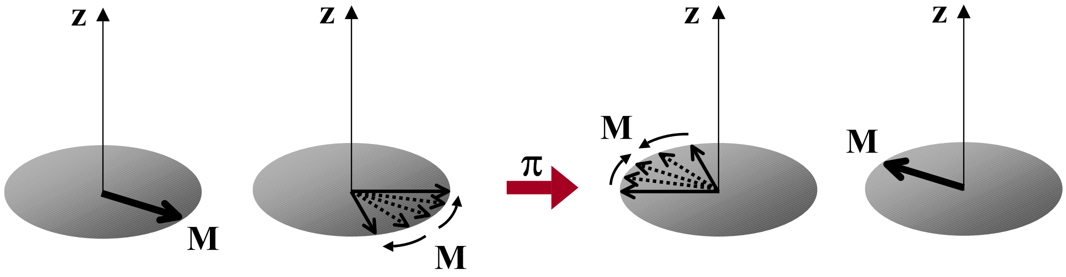

Figure 4.1: Creation of a spin echo.

be transformed into its complex conjugate M^* (Figure 4.1).[6] Therefore, after a 180-degree rotation, the transverse magnetization vector at time t will be

$$M(t) = \frac{1}{N}\sum_{j=1}^{N} \exp\left[+i\gamma \int_0^t b_j(\tau)d\tau\right] M^*(0). \tag{4.19}$$

If the spins continue to precess in the same sense they did before the application of the π pulse (in the runners' case, this would correspond to saying that the runners continue to run *forward* after they have turned around at time t), then, after an additional time t_1, they will acquire an extra phase, $\exp\left(-i\gamma\int_t^{t+t_1} b_j(\tau)d\tau\right)$, and the complex transverse magnetization in the rotating frame will be

$$M(t+t_1) = \frac{1}{N}\sum_{j=1}^{N} \exp\left[-i\gamma \int_t^{t+t_1} b_j(\tau)d\tau\right] \exp\left[+i\gamma \int_0^t b_j(\tau)d\tau\right] M^*(0). \tag{4.20}$$

For diffusing spins, the integrals over the field from 0 to t and from t to $t+t_1$ will not cancel out because spins diffuse randomly in the magnetic field. However, for stationary[7] spins, the integrals reduce to $\exp(-i\gamma b_j t_1)$ and $\exp(+i\gamma b_j t)$. Then,

$$M(t+t_1) = \frac{1}{N}\sum_{j=1}^{N} \exp\left[-i\gamma b_j(t_1 - t)\right] M^*(0). \tag{4.21}$$

---

[6] This can most easily be seen by fixing the axis of rotation and looking at the transformation of magnetization components under the 180-degree rotation. If the magnetization is rotated by 180° around the x-axis, for instance, then: $M_x \to M_x, M_y \to -M_y, M_z \to -M_z$. From this transformation we see that the complex transverse magnetization $(M_x + iM_y)$ transforms into its conjugate $(M_x - iM_y)$ under a 180-degree rotation around x, similarly for a 180-degree rotation around y-axis.

[7] Stationary spins are spins that do not move out of a voxel of size $(\Delta a)^3$, where Δa is the resolution of MR imaging system.

If $t = t_1$, then $M(2t) = M^*(0)$. This means that for stationary spins, the initial magnetization has been fully recovered at time $2t$. For diffusing spins, however, the echoes will still occur, but with progressively smaller amplitudes. The decay of the echoes due to diffusion will be examined in the next chapter.

In addition to signal loss due to diffusion of spins, the 180-degree pulses in the echo sequence do not refocus the effects of spin-spin interaction. To see this, we return to Eq. 4.18. For spin-spin interaction (see Section 4.4.2), the source of magnetic field b_j are the magnetic dipoles rather than the external field. By rotating the magnetization 180°, the magnetic dipoles and, therefore, the sources of the field inhomogeneity, are rotated as well. This means that in addition to converting the magnetization in Eq. 4.18 into its conjugate, the sign of b_j needs to be inverted. Consequently, the two exponentials do not cancel out–and the magnetization which was lost through the local fields of dipolar origin cannot be recovered [29].

Using the technique of spin echoes one can thus distinguish between the relaxation due to instrumentational limitations (i.e., inhomogeneous holding magnetic field) and relaxation inherent to the system (i.e., spin-spin interaction and diffusion). In other words, the $1/T_{\Delta B_z}$ term can be factored out of Eq. 4.2, so that

$$\frac{1}{T_2^*} = \frac{1}{T_{\Delta B_z}} + \frac{1}{T_2^{CPMG}}, \tag{4.22}$$

where the T_2^{CPMG} time constant describes the rate of spin echo decay resulting from the inherent T_2 relaxation and diffusion losses[8],

$$\frac{1}{T_2^{CPMG}} = \frac{1}{T_2} + \frac{1}{T_D}. \tag{4.23}$$

---

[8] CPMG stands for Carr-Purcell-Meiboom-Gill [69, 70].

4.4 Irreversible T2 Decay

The T2 relaxation which occurs due to magnetic field inhomogeneities can be removed using spin echo techniques. We call such relaxation a *reversible* T_2 decay. The spin-spin interactions and diffusion, on the other hand, contribute to an *irreversible* T2 decay, which will be examined in detail in this section.

4.4.1 Diffusion

We present two alternative approaches in deriving an expression for signal decay due to diffusion of spins in the field gradients. The first approach is statistical, based on the random walk of spins [59]. This approach illustrates the statistical nature of spins, but is cumbersome and limited to the case of constant gradients. The second approach is based on the generalized Bloch equation, which has two extra terms as compared to the standard Bloch equation–a term describing the transport of magnetization due to flow and a term describing the random transport of magnetization due to diffusion [59]. This approach is less intuitive, but has the advantage of being elegant and applicable to an arbitrary gradient form.

4.4.1.1 Statistical Approach to Signal Decay due to Diffusion in Constant Gradients

The goal is to find the average square phase shift $\overline{\Delta\theta^2}$ (Eq. 4.16) for spins diffusing randomly through a constant gradient. If the motion is limited to one dimension, then the frequency of precession of such spins is $\omega(t) = \gamma B_\circ + \gamma G x$, where x is the average distance that a particle travels in time t. If time t is divided into n steps, each of duration τ_s, then $t = n\tau_s$. During each step, the particle jumps either left or right with equal probability, so that $a_i = \pm 1$. If the root-mean-square (r.m.s.) displacement in one dimension is ξ, then the distance z travelled by the molecule after n jumps is

$$
\begin{aligned}
z(n\tau_s) &= \sum_{i=1}^{n} \xi a_i, &(4.24)\\
\overline{z^2(n\tau_s)} &= \sum_{i=1}^{n}\sum_{j=1}^{n} \xi^2 a_i a_j = \sum_{i=1}^{n}\sum_{j=1}^{n} \xi^2 \delta_{ij} = \sum_{i=1}^{n} \xi^2 = n\xi^2. &(4.25)
\end{aligned}
$$

Defining the diffusion constant as

$$D = \frac{\xi^2}{2\tau_s}, \tag{4.26}$$

we get

$$\overline{z^2(t)} = 2tD. \tag{4.27}$$

The above equation relates the macroscopic mean square displacement of a diffusing particle $\overline{z^2}$ and the diffusion constant D. For three-dimensional molecular motion, the factor 2 in Eq. 4.27 should be replaced by 6.

Let us go back to the equation describing the frequency of precession. Replacing x with $z(n\tau_s)$, we have

$$\omega(n\tau_s) = \gamma B_\circ + \gamma G \sum_{i=1}^{n} \xi a_i. \tag{4.28}$$

The cumulative angle after time $t = n\tau_s$ is

$$\phi(t) = \gamma B_\circ n\tau_s + \sum_{m=1}^{n} \gamma G\tau_s \sum_{i=1}^{m} \xi a_i = \phi_\circ + \Delta\phi. \tag{4.29}$$

Note that $\sum_{m=1}^{n} \gamma G\tau_s \sum_{i=1}^{m} \xi a_i = \sum_{i=1}^{n} (n+1-i)\xi a_i \gamma G\tau_s$. Therefore,

$$\begin{aligned}
\overline{\Delta\phi^2(n\tau_s)} &= \gamma^2 G^2 \tau_s^2 \xi^2 \sum_{i=1}^{n}\sum_{j=1}^{n}(n+1-i)(n+1-j)a_i a_j \\
&= \gamma^2 G^2 \tau_s^2 \xi^2 \sum_{i=1}^{n}\sum_{j=1}^{n}(n+1-i)(n+1-j)\delta_{ij} \\
&= \gamma^2 G^2 \tau_s^2 \xi^2 \sum_{i=1}^{n}(n+1-i)^2 = \gamma^2 G^2 \tau_s^2 \xi^2 \sum_{j=1}^{n} j^2 \\
&= \frac{1}{3}\gamma^2 G^2 \tau_s^2 \xi^2 n^3 \\
&= \frac{2}{3}\gamma^2 G^2 D \tau_s^3 n^3 \\
\overline{\Delta\phi^2(t)} &= \frac{2}{3}\gamma^2 G^2 D t^3,
\end{aligned} \tag{4.30}$$

where on line 3 of the above equation we used the equality $\sum_{i=1}^{n} (n+1-i)^2 = \sum_{j=1}^{n} j^2$.

If the average square phase shift is inserted into Eq. 4.16, we obtain an expression for the relaxation of the FID signal which results exclusively from the diffusion of spins in a constant gradient:

$$F(t) = \exp\left(-\frac{1}{3}\gamma^2 G^2 D t^3\right). \tag{4.31}$$

If a 180-degree RF pulse reverses the orientation of spins in the magnetic field gradients at time t, the spins begin to re-phase, until they are fully re-phased and an echo is formed at time $2t$ (see Section 4.3.1). The re-phasing of spins decreases the net effect of diffusion losses. In other words, if spins were allowed to diffuse in a positive (constant) gradient for a time $2t$, the diffusion losses would be proportional to $\exp\left[-\frac{1}{3}\gamma^2 G^2 D(2t)^3\right]$. However, since the π pulse reverses the sign of the magnetic field gradients seen by the spins at time t, the echo magnitude at time $2t$ will be

$$\begin{aligned} M(2t) &= M(t)\exp\left(-\frac{1}{3}\gamma^2 G^2 D t^3\right) \\ M(2t) &= \left[M(0)\exp\left(-\frac{1}{3}\gamma^2 G^2 D t^3\right)\right]\exp\left(-\frac{1}{3}\gamma^2 G^2 D t^3\right) \\ M(2t) &= M(0)\exp\left(-\frac{1}{12}\gamma^2 G^2 D\,(2t)^3\right). \end{aligned} \tag{4.32}$$

The spin echo at time $T = 2t$ can then be expressed as

$$M(T) = M(0)\exp\left(-\frac{1}{12}\gamma^2 G^2 D\,(T)^3\right). \tag{4.33}$$

4.4.1.2 Signal Decay due to Diffusion in an Arbitrary Gradient Waveform Based on the Bloch Equation

The generalized Bloch equation for the M_x-coordinate is

$$\frac{dM_x}{dt} = \gamma M_y B_{eff} - \frac{M_x}{T_2} + \nabla \cdot \vec{D} \cdot \nabla M_x - \nabla \cdot \vec{v} M_x. \tag{4.34}$$

The first term on the right hand side is due to the rotation of the magnetization around the effective field $B_{eff} = \left(B_\circ - \frac{\omega}{\gamma}\right) + \mathbf{r} \cdot \mathbf{g}$, where $\mathbf{g} = \partial B_z/\partial x\,\hat{\mathbf{dx}} + \partial B_z/\partial y\,\hat{\mathbf{dy}} + \partial B_z/\partial z\,\hat{\mathbf{dz}}$ is the magnetic field gradient and $\mathbf{r} = \mathbf{x} + \mathbf{y} + \mathbf{z}$ is the position of the spin with respect to an arbitrary origin; the second term represents the inherent T_2 relaxation; the third term stands for relaxation due to diffusion of spins in the magnetic field gradients; the fourth and last term represents relaxation due to the directional transport (i.e., flow) of magnetization.[9] By exchanging the subscript x in Eq. 4.34 with y and vice versa, one can obtain a similar

---

[9] We choose to include the ’flow’ term in the Bloch equation to illustrate the most general situation. Our *in vitro* experiments did not include flow; however, when modelling an *in vivo* situation, such as delivery of hyperpolarized gas to the lungs through inhalation, the relaxation due to the flow of magnetization should be taken into account.

equation for the M_y magnetization component:

$$\frac{dM_y}{dt} = -\gamma M_x B_{eff} - \frac{M_y}{T_2} + \nabla \cdot \vec{D} \cdot \nabla M_y - \nabla \cdot \vec{v} M_y. \tag{4.35}$$

We can combine Eqs. 4.34 and 4.35 by introducing a complex magnetization $M_+ = M_x + iM_y$. Furthermore, on resonance, $\omega = \gamma B_\circ$, and the effective field reduces to $B_{eff} = \mathbf{r} \cdot \mathbf{g}$. Thus,

$$\frac{\partial M_+}{\partial t} = -i\gamma \mathbf{r} \cdot \mathbf{g} M_+ - \frac{M_+}{T_2} + \nabla \cdot \vec{D} \cdot \nabla M_+ - \nabla \cdot \vec{v} M_+. \tag{4.36}$$

For isotropic diffusion, the diffusion term in the Bloch equation reduces to

$$\nabla \cdot \mathbf{D} \cdot \nabla M_+ = \nabla \cdot \begin{pmatrix} D & 0 & 0 \\ 0 & D & 0 \\ 0 & 0 & D \end{pmatrix} \cdot \nabla M_+ = D \nabla^2 M_+. \tag{4.37}$$

In addition, for spatially independent velocities, the flow term in the Bloch equation becomes

$$\nabla \cdot \vec{v} M_+ = (\nabla \cdot \vec{v}) M_+ + \vec{v} \cdot \nabla M_+ = \vec{v} \cdot \nabla M_+. \tag{4.38}$$

Assuming a solution of the form

$$M_+(\mathbf{r}, t) = A(t) \exp\left[-i\gamma \mathbf{r} \cdot \int_0^t \mathbf{g}(\tau) d\tau\right] \exp\left[-\frac{t}{T_2}\right], \tag{4.39}$$

and substituting it into Eq. 4.36, we get an expression for $A(t)$:

$$A(t) = \exp\left[-D\gamma^2 \int_0^t \left(\int_0^{t'} \mathbf{g}(\tau) d\tau\right)^2 dt'\right] \exp\left[i\gamma \mathbf{v} \cdot \int_0^t \left(\int_0^{t'} \mathbf{g}(\tau) d\tau\right) dt'\right]. \tag{4.40}$$

The first exponential on the right side of the above equation represents the signal decay due to diffusion, while the second exponential represents the signal decay due to flow. We will focus on the first term only. Since $k \equiv \frac{\gamma}{2\pi} \int_0^{t'} \mathbf{g}(\tau) d\tau$ [59], we can express the diffusion term as

$$\exp\left[-\frac{t}{T_D}\right] = \exp\left[-4\pi^2 D \int_0^t \mathbf{k}^2(t') dt'\right] = \exp\left[-Db\right], \tag{4.41}$$

where

$$b \equiv 4\pi^2 \int_0^t \mathbf{k}^2(\tau)d\tau. \tag{4.42}$$

Equation 4.41 tells us that by knowing the diffusion constant of the gas mixture and the integral of the gradient waveform over time, one can find T_D and as a result eliminate the signal decay due to diffusion from the total decay (see Eq. 4.2).

4.4.2 Spin-Spin Interaction

The theory of spin-spin interaction is very complex and can only be explained using the quantum mechanical description of nuclear interactions. We therefore limit this section to outlining the main steps in the derivation of T_2 as described in [59] .

There are several processes which contribute to dephasing of transverse magnetization [59]: the dipolar interaction between a pair of spins, chemical shift interaction, scalar coupling, and the quadrupole interaction (for $I > 1/2$). For spin-1/2 nuclei, the dominant interaction causing spin relaxation arises from the dipolar Hamiltonian [59], which is

$$H_D = \frac{\mu_\circ}{4\pi} \sum_{i<j} \frac{\gamma_i \gamma_j \hbar}{r_{ij}^3} \left[\mathbf{I}_i \cdot \mathbf{I}_j - \frac{3(\mathbf{I}_i \cdot \mathbf{r}_{ij})(\mathbf{I}_j \cdot \mathbf{r}_{ij})}{r_{ij}^2} \right], \tag{4.43}$$

where the sum refers to all the spin pairs (i,j), $\mathbf{I}$ is the vector operator given by $I_x\mathbf{x}+I_y\mathbf{y}+I_z\mathbf{z}$, and r_{ij} is the distance between two spins.

If we introduce a density matrix ρ, where for a spin-1/2 particle the density matrix is

$$\rho = \begin{bmatrix} \frac{1}{2} + \overline{\langle I_z \rangle} & \overline{\langle I_x - iI_y \rangle} \\ \overline{\langle I_x + iI_y \rangle} & \frac{1}{2} - \overline{\langle I_z \rangle} \end{bmatrix}, \tag{4.44}$$

then the evolution of the density matrix in the rotating frame of reference can be expressed as

$$i\frac{d\rho^*(t)}{dt} = \left[H_D^*(t),\, \rho^*(t)\right], \tag{4.45}$$

where H_D^* is the transformed dipolar Hamiltonian, $\exp[i\omega_\circ I_z t] H_D(t) \exp[-i\omega_\circ I_z t]$, $\rho^*(t)$ is transformed density matrix, $\exp[i\omega_\circ I_z t]\rho(0)\exp[-i\omega_\circ I_z t]$, and $\omega_\circ$ is the Larmor frequency.

Once the evolution of ρ^* in Eq. 4.45 is calculated, the decay of transverse relaxation can be determined. From [59], the transverse relaxation time in liquids T_2 is

$$\frac{1}{T_2} = \left(\frac{\mu_\circ}{4\pi}\right)^2 \gamma^4 \hbar^2 \frac{3}{2} I(I+1) \left[\frac{1}{4}J^{(0)}(0) + \frac{5}{2}J^{(1)}(\omega_\circ) + \frac{1}{4}J^{(2)}(2\omega_\circ)\right], \tag{4.46}$$

where $J^{(0)}(0)$, $J^{(1)}(\omega)$ and $J^{(2)}(\omega)$ are spectral density functions defined in terms of the rotational correlation time τ_c as

$$\begin{aligned} J^{(0)}(0) &= \frac{24}{15r_{ij}^6}\,\tau_c \\ J^{(1)}(\omega) &= \frac{4}{15r_{ij}^6}\,\frac{\tau_c}{1+\omega^2\tau_c^2} \\ J^{(2)}(\omega) &= \frac{16}{15r_{ij}^6}\,\frac{\tau_c}{1+\omega^2\tau_c^2}. \end{aligned} \tag{4.47}$$

4.5 Measurements of Reversible Transverse Relaxation with Free-Induction-Decay

The largest contribution to T_2^* relaxation is dephasing due to external field inhomogeneities (see Eq. 4.2), which can be removed using the technique of spin echoes. Consequently, T_2^* does not give any information about the system under study (hyperpolarized gas, for instance); it only describes how well one is able to *shim* the external magnet. To minimize the external field inhomogeneities, FID signals (which decay with time constant T_2^*, see Eq. 4.16) were collected prior to any other signal acquisition. Shimming currents were applied to the x, y, and z gradient coils in order to maximize T_2^* relaxation time. From the frequency domain perspective (see Appendix B), this translated into minimizing the linewidth of the frequency spectrum.

In addition to shimming, the FID signal was used to match the receiver frequency to the frequency of transmission (and therefore, precession). Special care was devoted to being within a few Hertz of the precession frequency to avoid off-resonance effects.

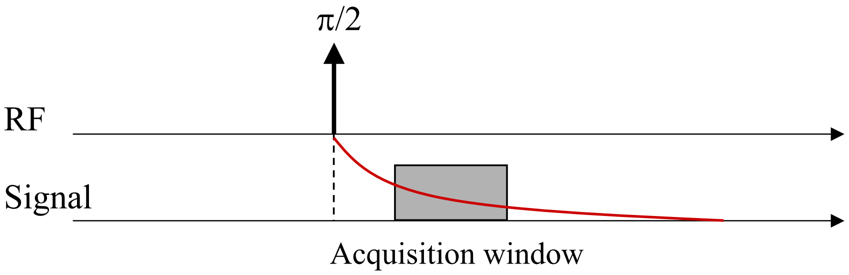

Figure 4.2: Pulse sequence used to generate free-induction-decay, or FID.

Figure 4.2 shows the basic structure of the pulse sequence used to generate free-induction-decay. The duration of the RF pulse determines the angle by which the magnetization has been tipped away from the static field (so-called “flip-angle”). If the amplitude of the RF field is B_1 and the frequency of precession around the B_1 field is $\omega_1 = d\theta/dt$, then the flip-angle $d\theta$ is

$$d\theta = \gamma B_1 dt. \tag{4.48}$$

Normally, the flip-angle is chosen to be 90° (i.e., $\pi/2$) to maximize the projection of magnetization onto the transverse plane and, therefore, the SNR.

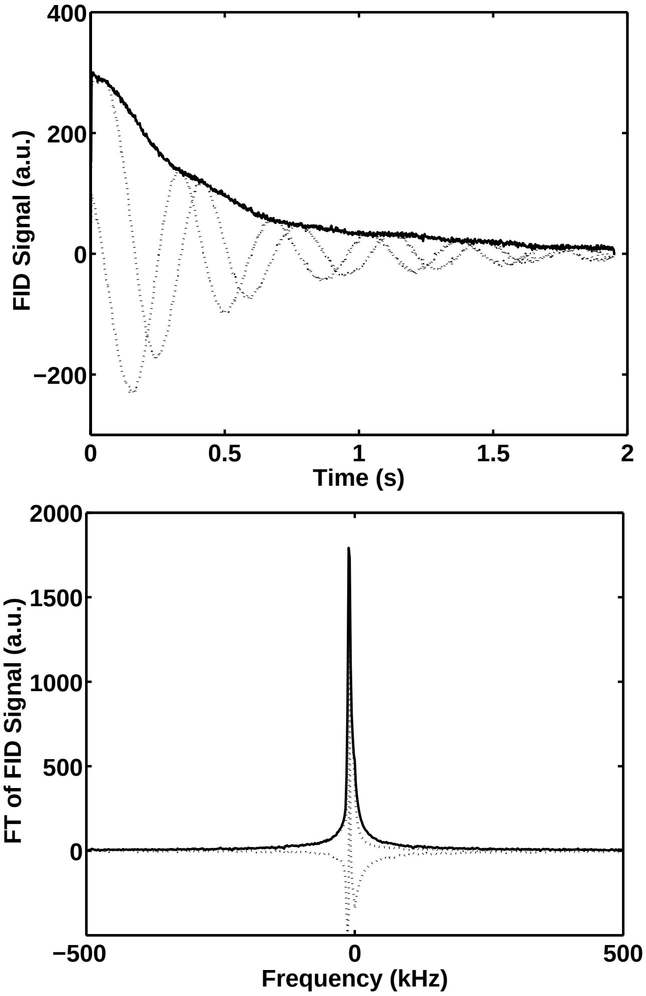

Figure 4.3: Free-induction-decay (FID) signal of water taken on the low-field pulsed resistive scanner (top) and its Fourier transform (bottom).

Figure 4.3 shows a typical FID signal of distilled water and its spectra, which is obtained by taking the Fourier transform (FT) of the time domain signal. Since the FT of an exponential decay is a Lorentzian (see Appendix B), we can fit the data to the function of the form

$$L(x) = \frac{1}{\pi} \frac{\frac{1}{2}\Gamma}{(\omega - \omega_\circ)^2 + \left(\frac{1}{2}\Gamma\right)^2}\,, \tag{4.49}$$

where Γ is the FWHM (Full-Width-Half-Maximum) value and $\omega_\circ$ is the central frequency of the fit. From Appendix B, the T_2^* relaxation time is

$$T_2^* = \frac{1}{\pi\Gamma}. \tag{4.50}$$

The typical linewidth (FWHM) of water, ^{129}Xe and ^{3}He frequency spectra at 397 kHz central frequency was between 5 and 15 Hz. The T_2^* relaxation rate for all samples was thus between 20 ms and 60 ms. Since the FID was collected from the entire sample (i.e., a sphere of diameter Δx, where $\Delta x = 2.5$ cm), the typical background gradients due to the field inhomogeneities were $G = \Delta f/(\gamma \Delta x) = 0.01 - 0.03$ mT/m.

4.5.1 Determination of Gas Polarization

Water and gas spectra were also used for calibrating the noble gas polarization. As demonstrated in Eq. 3.4, the NMR signal is proportional to the magnetization of the sample and the frequency ω at which the signal was acquired (i.e., readout frequency). The magnetization of the sample can be expressed in terms of the polarization as $M = Pn\mu$, where n is the number density of the sample and μ is its magnetic moment. Therefore,

$$\frac{S_{Hyp\,Gas}}{S_{H_2O}} = \frac{P_{Hyp\,Gas}}{P_{H_2O}} \; \frac{n_{Hyp\,Gas}}{n_p} \; \frac{\mu_{Hyp\,Gas}}{\mu_p} \; \frac{\omega_{Hyp\,Gas}}{\omega_{H_2O}}, \tag{4.51}$$

where the subscript *HypGas* refers to either ^{129}Xe or ^{3}He, n_p is the proton number density and μ_p is the proton magnetic moment. By measuring the ratio of the hyperpolarized gas and water signals which were acquired at the same readout frequency, the noble gas (hyper)polarization can be evaluated from

$$P_{Hyp\,Gas} = P_{H_2O} \; \frac{n_p}{n_{Hyp\,Gas}} \; \frac{\mu_p}{\mu_{Hyp\,Gas}} \; \frac{S_{Hyp\,Gas}}{S_{H_2O}}. \tag{4.52}$$

The ratio of magnetic moments can be determined immediately: $\mu_p = 2.793\mu_N$, $\mu_{Xe} = 0.780\mu_N$, and $\mu_{He} = 2.127\mu_N$, where μ_N is the nuclear magnetic moment. Therefore, $\mu_p/\mu_{Xe} = 3.58$ and $\mu_p/\mu_{He} = 1.31$.

The number density is commonly expressed in units of *amagat*, which is defined as the number density per standard atmosphere ($p = 1$ atm, $T = 273$ K). Thus, from the ideal gas law ($pV = nRT$, where R is the universal gas constant), 1 amagat = 44.50 mol/m^3. For water at $T = 25$°C,

$$n_{H_2O} = \frac{\rho_{H_2O}\left[\frac{\mathrm{g}}{\mathrm{m}^3}\right]}{\rho_{H_2O}^{molar}\left[\frac{\mathrm{g}}{\mathrm{mol}}\right]} \; \frac{[\mathrm{amagat}]}{44.50\left[\frac{\mathrm{mol}}{\mathrm{m}^3}\right]}\,. \tag{4.53}$$

Since at $T = 25$°C, $\rho_{H_2O} = 997 \times 10^3$ g/m^3, and $\rho_{H_2O}^{molar} = 18$ g/mol, it follows that

$n_{H_2O} = 1244.69$ amagats. Because there are two protons in each water molecule, the proton number density is $n_p = 2489.4$ amagats.

For hyperpolarized gas, the number density in *amagats* is a function of the gas pressure $p_{Hyp\,Gas}$ normalized to 1 atm; the temperature of the gas when the cells were filled, $T_{Hyp\,Gas}$, normalized to 273 K; and the abundance F of the spin-1/2 gas in the gas mixture:

$$n_{Hyp\,Gas} = \frac{p_{Hyp\,Gas}\,[\mathrm{atm}]}{1\,[\mathrm{atm}]}\,\frac{273\,[\mathrm{K}]}{T_{Hyp\,Gas}\,[\mathrm{K}]}\,F_{Hyp\,Gas}\,[\mathrm{amagat}]\,. \tag{4.54}$$

The xenon cell used for hyperpolarized ^{129}Xe experiments was filled with 0.48 atm of naturally abundant ^{129}Xe ($F_{Xe} = 26.44\% = 2.644 \times 10^{-3}$) at room temperature (300 K). The ^{129}Xe number density in the cell was thus $n_{Xe} = 0.115$ amagats. The helium cell used for all the hyperpolarized ^{3}He experiments was filled with 0.74 atm of pure ^{3}He ($F = 100\% = 1$) at room temperature. Therefore, the number density of ^{3}He in the cell was $n_{He} = 0.6825$ amagats. Table 4.1 summarizes the gas content of the cells.

	Hyp Gas Pressure (atm)	Nitrogen Pressure (atm)
^{129}Xe Cell	0.48	0.14
^{3}He Cell	0.75	0.10

Table 4.1: The gas content of ^{129}Xe and ^{3}He cells used at Stanford. All pressures measured at room temperature.

The thermal polarization of water protons is equal to the fraction of protons which are in the lower energy state , $N\uparrow/N_{total}$, minus the fraction of protons that are in the upper energy state, $N\downarrow/N_{total}$:

$$P^{thermal}_{H_2O} = \frac{N\uparrow - N\downarrow}{N\uparrow + N\downarrow}. \tag{4.55}$$

Using the Boltzmann distribution, we can express the number of protons in the lower energy state in terms of the number of protons in the higher energy state:

$$N\uparrow = N\downarrow \exp\left(\frac{\Delta E}{kT}\right) = N\downarrow \exp\left(\frac{\hbar\gamma B_\circ}{kT}\right). \tag{4.56}$$

Substituting this relation into Eq. 4.55 we get

$$P = \left[\frac{1 - \exp\left(-\hbar\gamma B_\circ / kT\right)}{1 + \exp\left(-\hbar\gamma B_\circ / kT\right)} \right] = \tanh\left(\frac{\hbar\gamma B_\circ}{2kT} \right). \tag{4.57}$$

At high temperatures T or small magnetic fields $B_\circ$ the hyperbolic tangent can be expanded in a power series. If only the first power term is kept, the thermal polarization becomes

$$P \sim \frac{\hbar\gamma B_\circ}{2kT} = \frac{\mu_p B_\circ}{kT}, \tag{4.58}$$

since $\Delta E = 2\mu_p B_\circ = \hbar\gamma B_\circ$ for a spin 1/2 particle. Notice that $\mu_p = 8.8 \times 10^{-11}$ eV/mT, $kT = 0.0258$ eV at room temperature, and $B_\circ = 397$ kHz/42.58 $\frac{\text{kHz}}{\text{mT}}$. The thermal polarization of water at room temperature and 397 kHz readout frequency is thus $P_{H_2O} = 3.18 \times 10^{-8}$.

It only remains to evaluate the ratio of hyperpolarized gas and water signals. We collected FID signals of distilled water using no polarizing waveform, so that the signal was entirely due to the thermal polarization at the readout frequency (397 kHz). Since the longitudinal relaxation time–which characterizes the rate of growth of thermal polarization in the applied magnetic field–was measured to be around 2.4 s for distilled water, we started signal acquisition approximately $3T_1$ or 7 s after the application of the readout pulse. This "waiting period" enabled the protons to reach thermal equilibrium levels before the collection of the FID signal. The hyperpolarized gas and water FID signals were collected using 90-degree flip-angles for maximum SNR.

Both water and hyperpolarized FID signals were Fourier transformed into the frequency domain and then analyzed using Matlab. First, the DC background level of both spectra was estimated using a linear fit through the noise tails (see Figure 4.4 and 4.5) and then subtracted from the main signal magnitude. This procedure removed any undesired impulse which could have appeared in the time domain signal at $t = 0$ as a result of electronic circuitry.[10] The areas under the gas and water spectral curves were then estimated by integrating the spectral function from one noise tail to the other. Finally, the gas polarization was estimated using Eq. 4.52.

We also compared the noise levels of water and hyperpolarized gas signals. In principle,

---

[10] One possible source of the impulse at $t = 0$ is the digital filter which could be coupling the switching noise into the AD converter.

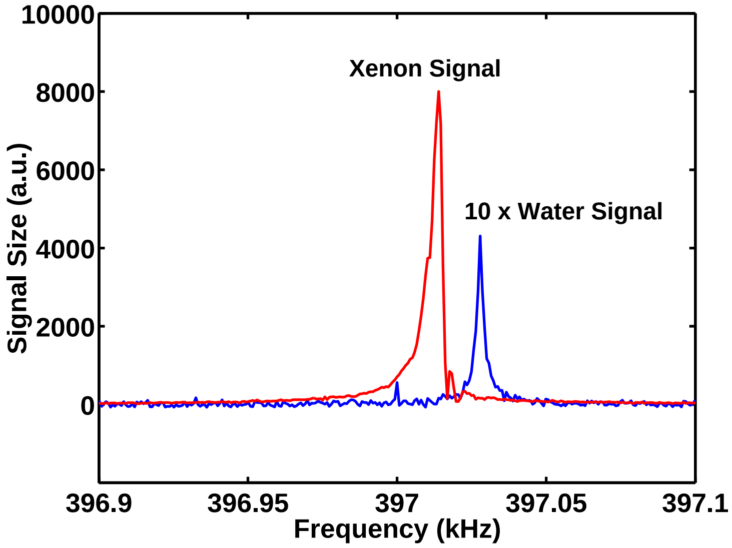

Figure 4.4: Xenon and water spectra used to calibrate xenon polarization levels.

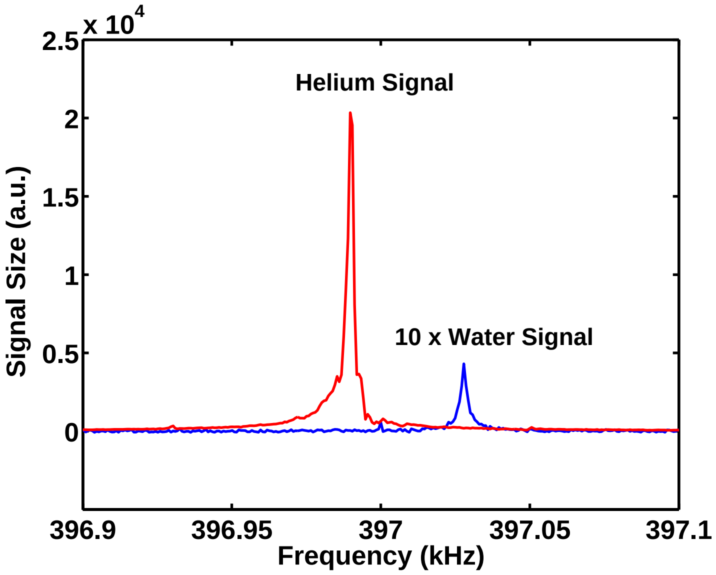

Figure 4.5: Helium and water spectra used to calibrate helium polarization levels.

if the water and gas signals were obtained on the same day, under the same conditions, the noise levels of both signals should have been comparable in size, because the dominant source of noise at the readout frequency of 397 kHz was the coil, which was the same for both samples. Therefore, a mismatch in the water and gas noise levels could indicate that the low-field pulsed resistive system response has changed after the collection of one spectra and before the collection of the other. One possibility is phase noise, which is a consequence of variations in the phase of the readout magnet that result when the magnet heats up. Unfortunately, phase noise is a function of signal size and thus can change the SNR response of the system. It is thus impossible to retroactively correct the signal size by scaling the signals with the ratio of noise levels. The noise levels of water and hyperpolarized gas in our measurements were within 70% of each other, which means that the ratio of hyperpolarized gas and water areas is at best 30% accurate. The errors in estimating other factors in Eq. 4.52 are negligible compared to the error in the estimation of the areas. The calibration of noble gas polarization is thus 30% accurate. This level of accuracy was satisfactory, since our goal at Stanford was not precise polarimetry, but to explore the versatile function of the low-field pulsed resistive system in imaging water and hyperpolarized gas.

Figure 4.4 shows ^{129}Xe and water spectra plotted on the same scale, while Figure 4.5 shows ^{3}He and water spectra. The typical ^{129}Xe polarization after 5 min of pumping with 7 W of circularly polarized laser power was between 2% and 7%, while after 30 min of pumping with 7 W of laser power we were able achieve polarizations of around 1% for ^{3}He.

4.5.2 Adiabatic Condition for Spin Transition in the Pulsed Scanner

Unlike water, which requires a polarizing field to increase its thermal polarization levels, the hyperpolarized gas polarization is created by the optical pumping process and thus does not require a polarizing waveform in the pulse sequence. Therefore, in the hyperpolarized gas experiments, only the readout field $B_{\circ}$ was used. However, due to its pulsed nature, the readout field is constantly turned *on* and *off* during imaging. While *off*, the noble gas magnetization is aligned with the Earth's field, which in the low-field pulsed resistive scanner is not parallel to the readout field. In contrast, during the *on* state, the magnetization aligns with the readout field which is two orders of magnitude bigger than the Earth's field. If this transition (see Figure 4.6) were nonadiabatic, significant polarization losses could occur.

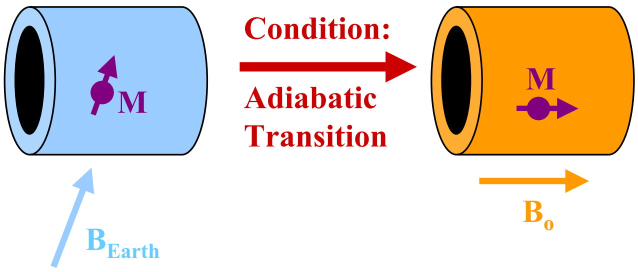

Figure 4.6: A schematic representation of the hyperpolarized gas magnetization alignment during imaging on the low-field pulsed resistive scanner. Left: magnetization alignment before the application of $B_\circ$ field. Right: magnetization alignment after the application of $B_\circ$ field. An adiabatic transition between the two states is required to prevent polarization loss.

We now compute the maximum ramping speed of the readout field allowed by the adiabatic condition. The adiabatic condition dictates the rate of change of the angle between the Earth's field B_E and the effective field $B_{eff}(t)$ (Figure 4.7). In the worst-case scenario, the Earth's field and the readout field are orthogonal.[11] The angle θ between B_{eff} and B_E can be expressed in terms of the time-varying readout field $B_\circ = tB_{max}/T_{ramp}$, where B_{max} is the saturation value of the readout field and T_{ramp} is the time it takes the readout field to reach its saturation value (see Figure 4.7),

$$\theta(t) = \arctan\left(\frac{tB_{max}}{T_{ramp}B_E}\right) \equiv \arctan\left(\frac{t}{\alpha}\right), \tag{4.59}$$

where $\alpha \equiv \frac{T_{ramp}B_E}{B_{max}}$. Thus,

$$\dot{\theta}(t) = \frac{\alpha}{(t^2+\alpha^2)}. \tag{4.60}$$

The transition will be adiabatic if the frequency of precession around the effective magnetic field is much bigger than the rate of change of θ. Therefore, $\dot{\theta}(t) \ll \gamma B_{eff}$, where

$$\gamma B_{eff} \quad = \quad \gamma\left[B_\circ^2(t) + B_E^2\right]^{1/2}$$

---

[11] Even though the Earth's field was not orthogonal to the readout field in the low-field pulsed resistive scanner, the worst-case scenario is a valid scenario at the beginning of the ramping period, when $B_\circ(t<0) = 0$. The readout field ramping time which we derive in this section can be viewed as an upper limit on the ramping time that allows an adiabatic change of magnetization alinement. The ramping time could be shorter if we created a special readout-field pulse.

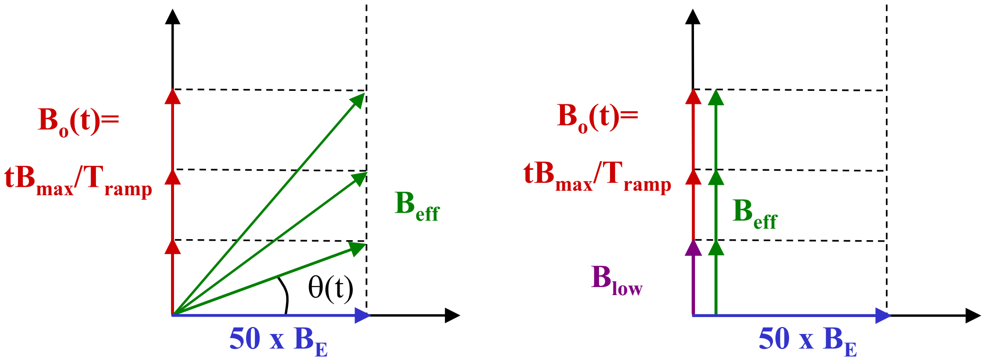

Figure 4.7: A vectorial representation of the hyperpolarized gas magnetization transition during the ramping of the readout field. Left: Without the background field. Right: With small background field, $\mathbf{B_{low}}$, along z-direction.

$$\begin{aligned} &= \gamma\left[\left(\frac{B_{max}t}{T_{ramp}}\right)^2 + B_E^2\right]^{1/2} \\ &= \gamma\frac{B_{max}}{T_{ramp}}\sqrt{t^2+\alpha^2}. \end{aligned} \tag{4.61}$$

The adiabatic condition can also be expressed as a ratio,

$$\frac{\dot{\theta}(t)}{\gamma B_{eff}(t)} = \frac{\alpha^2}{\gamma B_E\left[t^2+\alpha^2\right]^{3/2}} \ll 1. \tag{4.62}$$

Worst case occurs when $t = 0$. Thus,

$$\begin{aligned} \frac{\dot{\theta}(0)}{\gamma B_{eff}(0)} = \frac{1}{\gamma B_E \alpha} &\ll 1 \\ \Rightarrow T_{ramp}\left(\frac{B_E}{B_{max}}\right) &\gg \frac{1}{\gamma B_E}\,. \end{aligned} \tag{4.63}$$

In our case, $B_E \approx 50\ \mu$T and $B_{max} = 25$ mT. Hence,

$$\begin{aligned} T_{ramp} &\cong 200 \text{ ms for } {}^{3}\text{He} \\ &\cong 600 \text{ ms for } {}^{129}\text{Xe}. \end{aligned} \tag{4.64}$$

The results tell us that the magnetization will change adiabatically if the initial ramp-up time of the readout field is at least 200 ms long for ^{3}He and 600 ms long for ^{129}Xe. However, T_{ramp} is limited by the magnet rise-up time L/R, where L and R are the coil's inductance and resistance, respectively. For the readout magnet, the rise-up time is approximately 50 ms–a time too short for the adiabatic transition of hyperpolarized gas magnetization. A different method was thus needed to achieve an adiabatic sweep.

The problem was solved by applying a small offset current to the readout magnet in order to dominate the Earth's field and prevent the angle change during the *off* state of the readout field. The situation is illustrated on the right side of Figure 4.7. In this new operational mode, the readout magnet was never completely *off*–it was either on a high mode setting (which determines the readout frequency) or on a low mode setting (typically, 1 mT). A modified pulse sequence is shown in Figure 4.8.

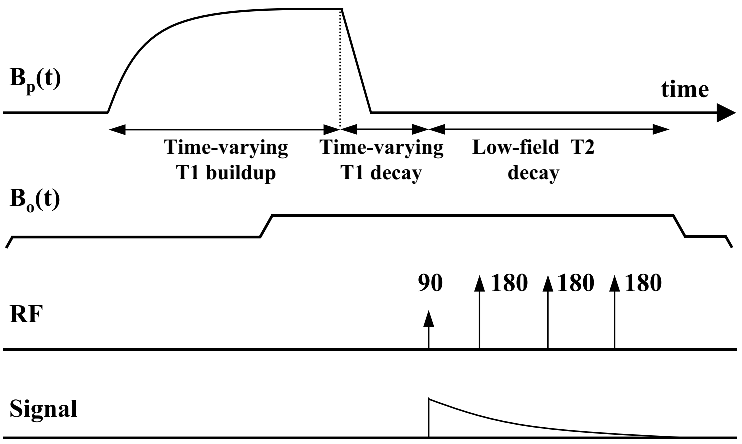

Figure 4.8: Timing diagram of a typical PMRI pulse sequence with a modified $B_\circ$ waveform. Unlike in the diagram of Figure 3.2, the $B_\circ$ is now on a low-field setting before the application of the B_p pulse.

To demonstrate experimentally that a fraction of polarization is lost without the low field enabled during the *off* mode of the readout magnet, we performed measurements of FID amplitude with and without the background (low) field present. We observed anywhere between 30% to 70% loss in hyperpolarized magnetization when the low-field setting was disabled. The wide spread in measurements was due to our inability to control precisely the parameters which affect the initial value of the gas magnetization, such as the time it takes to walk the cell from the pumping setup into the imaging scanner. Using this method we were also not able to determine accurately the minimal value of the low field required to prevent magnetization losses. Instead, we performed an experiment which gave a negative result (i.e., no signal) when the low field was *on*, and a positive result (i.e., signal) when the low field was *off*.

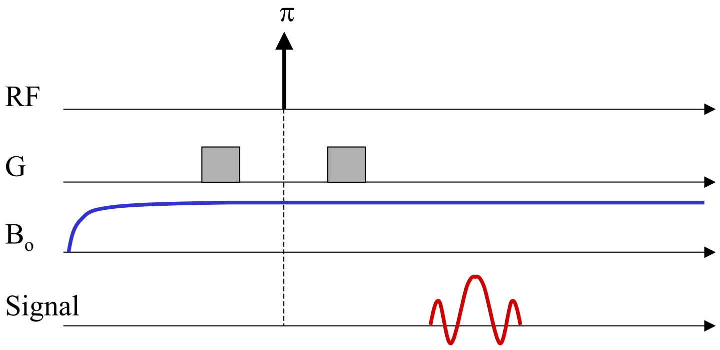

Figure 4.9: Pulse sequence used for demonstrating the non-adiabatic ramp-up of $B_\circ$ pulse in the absence of the low-field setting.

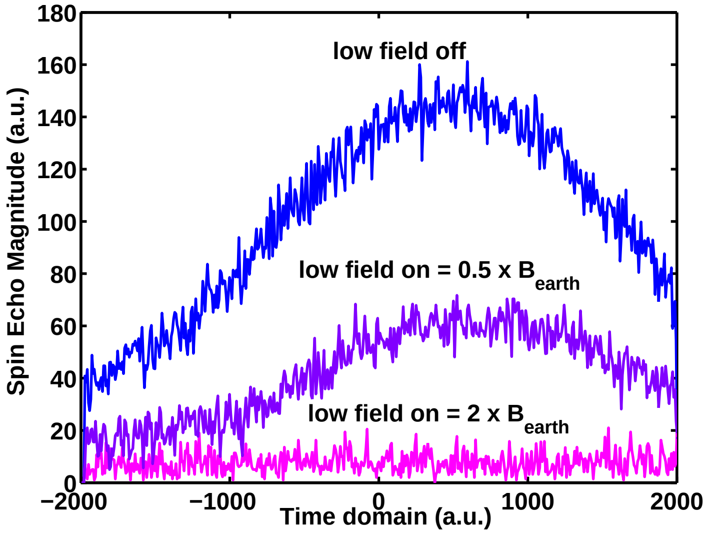

Figure 4.10: Creation of spin echoes demonstrating the existence of transverse magnetization before the ramp-up of the $B_\circ$ pulse: without the background field, with background field = 25 μT and with background field = 100 μT.

The experiment relied on the creation of a spin echo using a 180-degree pulse, a technique we described in Section 4.3.1. Figure 4.9 shows the sequence used in the experiment. Notice that there is no 90-degree pulse in this sequence, which would normally flip the magnetization from the z-axis on to the xy plane. Nevertheless, a spin echo was created after the 180-degree pulse. This indicated the presence of transverse magnetization before the (non-adiabatic) ramp-up of the $B_\circ$ field. On the other hand, if the low-field setting was enabled, the magnetization was aligned entirely along the z-direction before the ramp-up of the $B_\circ$ field, and consequently, no echo was formed. A small “crusher” (i.e., destructive) gradient was applied to destroy the FID signal which would result from an imperfect 180-degree pulse.

Figure 4.10 shows the results of spin echo experiments, confirming the need for the low-field setting during the *off* mode of the readout field cycle. When the low field was smaller than 0.1 mT (twice the Earth’s field), an echo was created, which proves that transverse magnetization existed before the ramp-up of $B_\circ$ field. This transverse magnetization would have either been lost after the non-adiabatic ramp-up or, in the case of spin echo sequence, could contribute to the creation of stimulated echoes. From the results in Figure 4.10 we were able to conclude that the minimum (critical) field needed to prevent polarization loss was 0.1 mT. The low field used in our experiments was 1 mT, which is well above the critical value.

4.6 Measurements of Irreversible Transverse Relaxation Using CPMG Sequence

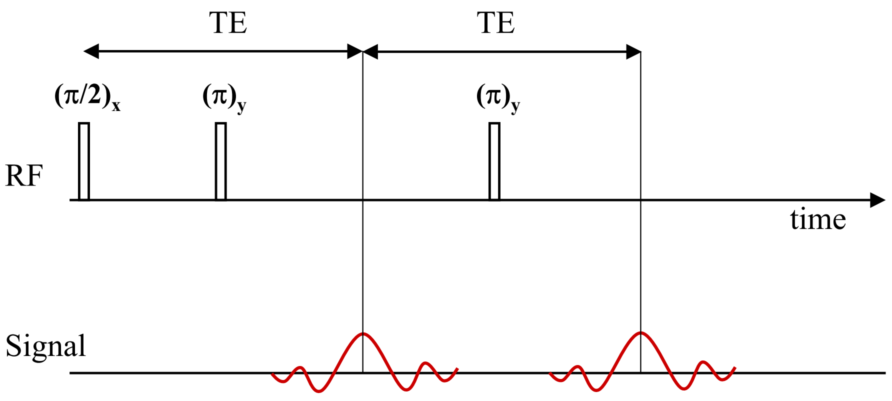

Figure 4.11: Pulse sequence used to generate a Carr-Purcell-Meiboom-Gill echo train.

The irreversible T_2 relaxation, given by the Eq. 4.23, describes the decay of a spin echo train in a Carr-Purcell-Meiboom-Gill sequence. The basic sequence used to create a spin echo train is illustrated in Figure 4.11. First, a 90-degree pulse was applied along one of the transverse axis (either x or y). A time $TE/2$ later, a 180-degree pulse was applied along the other transverse axis (either y or x). The 180-degree pulse flips the spins in the transverse plane (around either y or x axis) and causes a spin echo to appear at time TE after the application of the 90-degree pulse. By reapplying the 180-degree pulses in equally spaced intervals of length TE, an echo gets created each time at a half point ($TE/2$) between the 180-degree pulses. Since TE equals the length between two successive echoes, it is also called “interecho time”. The axis of rotation of the 180-degree pulses (which is related to the phase of the RF pulses) has to be parallel to the orientation of magnetization [29]. For instance, after the application of a 90-degree pulse which rotates the spins around the x-axis, the spins are aligned along the y-axis; consequently, the 180-degree pulses have to be applied along the y-axis. This algorithm prevents the accumulation of errors from imperfect 180-degree pulses.

Figure 4.12 shows an example of ^{3}He and ^{129}Xe spin echo trains obtained on the low-field pulsed resistive scanner. Each plot contains 32 echoes. The interecho time for ^{3}He was 57.03 ms, while the TE for ^{129}Xe was 67.34 ms. There is nothing fundamental about the

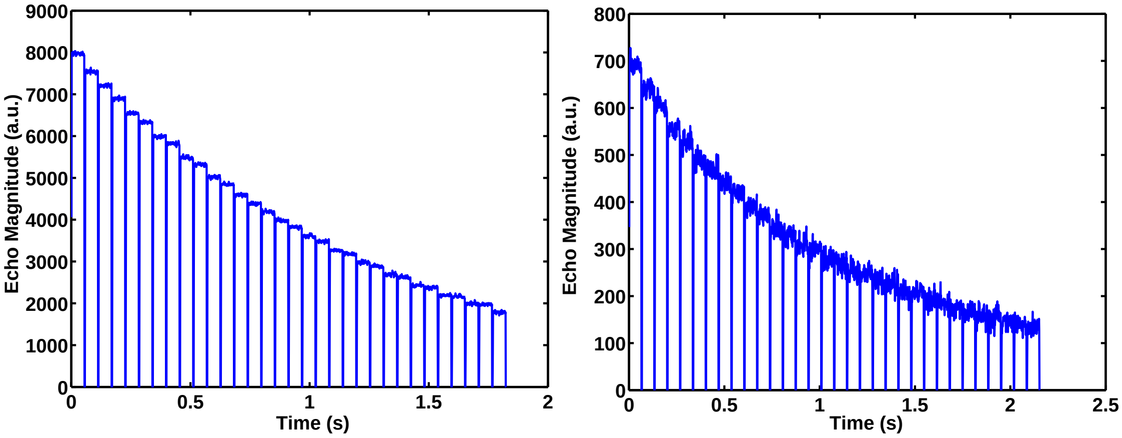

Figure 4.12: ^{3}He (left) and ^{129}Xe (right) spin echo trains obtained with the CPMG sequence.

TE times used in these experiments. The TE values were chosen so that we could display clearly the T_2^{CPMG} relaxation experienced by the gas during the acquisition window.

To extract the T_2^{CPMG} time constant from the echo trains such as the ones shown in Figure 4.12, we perform a least-square fit to the logarithm of the data.[12] The fit is a straight line of the form

$$\ln(S) = -\frac{t}{T_2^{CPMG}} + \ln S_\circ \rightarrow y = -tk + n, \tag{4.65}$$

where $y = \ln S$ is the natural log of the average (mean) echo magnitude, which was obtained by integrating the area under each echo; $n = \ln S_\circ$ is the natural log of the initial echo magnitude; and $k = 1/T_2^{CPMG}$ is the relaxation rate of the spin echo train in the CPMG sequence. Figure 4.13 shows experimental data as well as the fit to the data (using Eq. 4.65) of average echo magnitude as a function of time during a CPMG sequence. The T_2^{CPMG} relaxation time obtained from the fit was 49.5 s.

Measurements of T_2^{CPMG} showed a strong dependence of T_2^{CPMG} relaxation time on the interecho time TE. Consequently, unique ^{3}He and ^{129}Xe T_2^{CPMG} relaxation times do not exist. However, the dependence of T_2^{CPMG} on the interecho time is important for determining the inherent T_2 relaxation rate of gases, which is the subject of Section 4.8. In that section we study the functional dependence of T_2^{CPMG} on TE and develop a method for extracting the inherent T_2 relaxation time from the T_2^{CPMG} data.

In the following two subsections we examine in more detail two common problems en-

---

[12] In Matlab, the least-square algorithm is implemented into the function *polyfit* which we used for fitting the data.

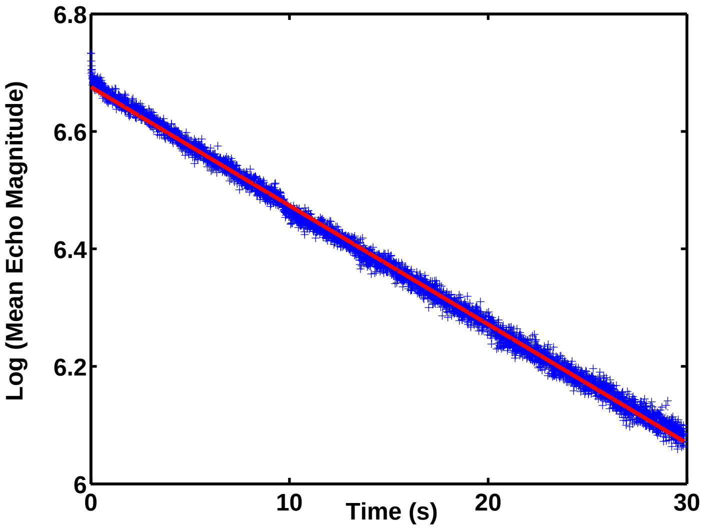

Figure 4.13: A logarithmic plot of the average measured ^{129}Xe spin echo magnitude as a function of time and best fit to the data. Number of echoes=4096, TE=7.29 ms, T2 extracted from the plot=49.5 s.

countered when using the CPMG spin echo sequence on the low-field pulsed resistive scanner: the generation of stimulated echoes and the off-resonance effects resulting from the resistive heating of the magnet.

4.6.1 Errors in RF Pulse Calibration and Stimulated Echoes

The duration of the RF pulses determines the magnetization flip-angle according to the Eq. 4.48. The magnitude of B_1 field in Eq. 4.48 is a function of the shape and size of the RF coil, the strength of the current in the coil, and the position of the sample within the coil. If the sample *fills* the coil (i.e., the coil fits tightly around the sample), the magnitude of B_1 can vary significantly across the sample. For all these reasons, the magnitude of B_1 is not known *a priori* and the flip-angle calibration has to be determined experimentally. The common procedure is to look for a null in the FID signal–a result of a 180-degree flip–while systematically increasing the duration of the B_1 pulse. However, this method is not practical for hyperpolarized gases since $(M_\circ \sin\alpha)$ of noble gas magnetization is destroyed after each α-degree pulse. We therefore always calibrate the RF pulses on a water phantom and then scale the duration of the B_1 pulse by the ratio of gas and water gyromagnetic moments. For a flip-angle α, the duration of the B_1 field in the case of hyperpolarized gas,

$T_\alpha^{Hyp\,Gas}$, and in the case of water, $T_\alpha^{H_2O}$, are related by

$$\begin{aligned} \alpha &= \gamma_p\, B_1\, T_\alpha^{H_2O} = \gamma_{Hyp\,Gas}\, B_1\, T_\alpha^{Hyp\,Gas} \\ &\rightarrow\; T_\alpha^{Hyp\,Gas} = \frac{\gamma_p}{\gamma_{Hyp\,Gas}}\, T_\alpha^{H_2O}. \end{aligned} \tag{4.66}$$

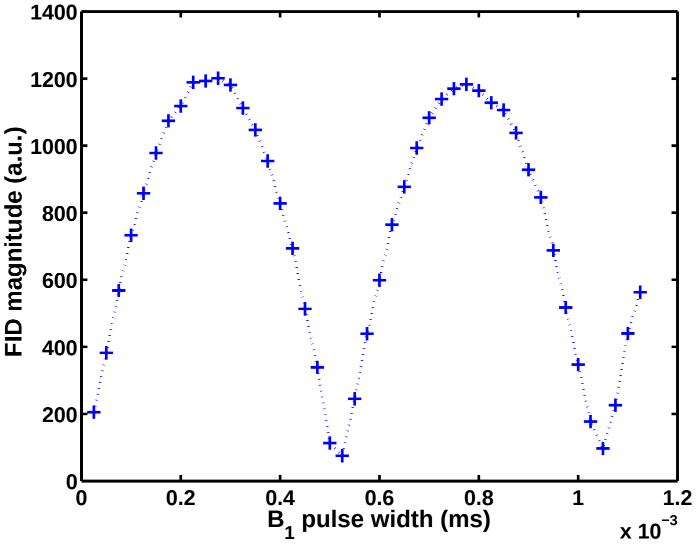

Figure 4.14: Measurement of FID magnitude as a function of B_1 pulse duration.

Figure 4.14 is an example of RF pulse calibration. It displays the magnitude of the FID signal at time $t = 0$ as a function of B_1 pulse width. As predicted from

$$M_{xy} = M_\circ \left|\sin\left(\gamma B_1 T_\alpha\right)\right|, \tag{4.67}$$

the dependence of the FID magnitude on the B_1 pulse width is sinusoidal. The maximum FID values correspond to odd multiples of $\pi/2$ (90° and 270°), while the nulls correspond to even multiples of $\pi/2$ (180° and 360°). Measurements such as this one enabled us to determine the width of B_1 for any flip-angle.

One of the implication in using the above-described calibration procedure is that any error in measuring the width of the 180-degree pulses translated into an error in the RF flip-angle. The accuracy in determining the width of a 180-degree pulse when looking for a null in the FID signal was ±1 μs. The width of the 180-degree pulse depended on the signal attenuation used in producing the magnitude of B_1 pulse. With the attenuation most commonly used, the length of 180-degree pulse for water was around 120 μs. Thus, the error in the RF flip-angle could be as high as 0.8%-1%. This means that in the CPMG sequence, around $\sin(180 - 0.01 \times 180) = 3\%$ of the initial magnetization might end up along the longitudinal axis after each 180-degree pulse. This would cause an accelerated decay of the transverse component M_{xy}. In addition, the magnetization stored along the longitudinal axis would eventually be knocked back into the transverse plane by an imperfect 180-degree pulse and contribute to the creation of stimulated echoes. Such echoes were observed occasionally during our measurements. Figure 4.15 shows an example of an echo train that produced stimulated echoes in the second half of the train. We attribute this effect to miscalibrated 180-degree pulses.

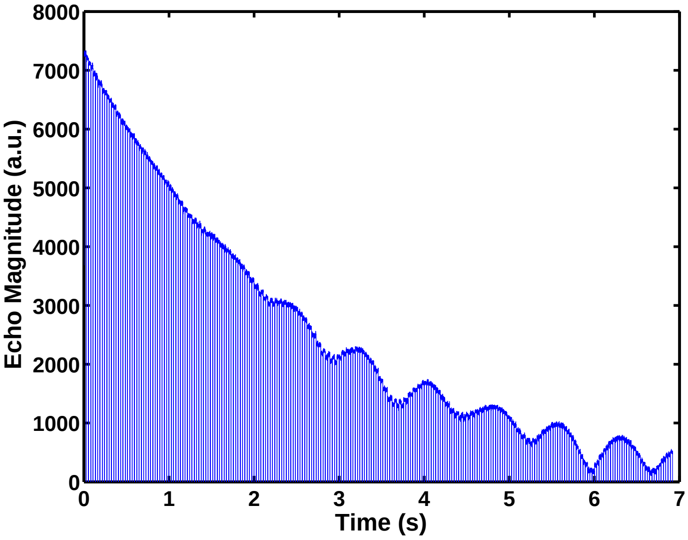

Figure 4.15: An example of the occurrence of stimulated echoes during a CPMG spin echo train. Number of echoes=256, TE=27.03 ms.

4.6.2 Heating of the Magnet and Off-Resonance Effects

One of the challenges in using resistive magnets for MR imaging is temporal instability of the magnetic field due to the resistive heating of the copper wires. The heat causes the copper wires to expand outward from the center of the magnet bore–a process, which changes the strength of the magnetic field at the position of the sample. In addition, the increase in the temperature of the wires increases their resistance and, as a result, the power of the magnetic field changes. The temporal instability of the $B_\circ$ field causes drifts in the readout frequency and therefore, phase errors. In Section 3.4.1 we showed that for a field-of-view of 10 cm and a resolution of 1 mm, the temporal stability of the magnet should be better than 100 ppm.

The temporal drifts in the readout field are particularly damaging in the case of CPMG sequence, which has stringent phase stability requirements. In Section 4.3.1 we derived an expression (Eq. 4.20) for the complex transverse magnetization in the rotating frame after the application of a 180-degree pulse, for the case of time-dependent local fields b_j. In that derivation we made an assumption that stationary spins (unlike freely diffusing spins) see a constant, time-independent field, which enabled us to solve the integral in Eq. 4.20. That assumption no longer holds when the local fields change due to temporal instabilities arising from resistive heating of the magnet. In such a case, the two exponential terms in Eq. 4.20 no longer cancel out. The situation is conceptually similar to the case of diffusing spins; the only difference is in the source of the temporal field variation.

To solve the time integrals in Eq. 4.20, we need to make an assumption about the form of the $b_j(\tau)$ field. To first order, the field drifts linearly with time, so that $b_j(\tau) = b_\circ + \alpha t$, where $b_\circ$ is the Larmor frequency of the individual spin, and $\alpha = \partial b/\partial t$. Equation 4.20 then reduces to

$$\begin{aligned} M(2t_1) &= \frac{1}{N}\sum_{j=1}^{N} \exp\left[-i\gamma\alpha_j t_1^2\right] M^*(0) \\ M(t) &= \frac{1}{N}\sum_{j=1}^{N} \exp\left[-\frac{i}{4}\gamma\alpha_j t^2\right] M^*(0). \end{aligned} \tag{4.68}$$

Assuming all spins see the same field variation $\partial b_j/\partial t \equiv \partial B/\partial t$, the sum over all spins reduces to

$$M(t) = \exp\left[-\frac{i}{4}\frac{\partial(\gamma B)}{\partial t} t^2\right] M^*(0). \tag{4.69}$$

The above equation represents the complex magnetization at time t in terms of the initial magnetization (at $t = 0$). We see that unlike in the case of time-independent field, the echo for a linearly drifting field is phase shifted with respect to the original signal. As a result, the axis of rotation is no longer parallel to the magnetization–a situation which violates the CPMG condition (see beginning of Section 4.6). As the echo train progresses, transverse phase errors diverge. This leads to the growth of the longitudinal magnetization, a faster decay of transverse magnetization and, potentially, to stimulated echoes, as discussed in Section 4.6.1.

Measurements of T_2^{CPMG} presented in Section 4.6 (see Figure 4.13) demonstrate that our resistive system can maintain sufficient temporal stability to acquire as many as 4096 echoes in the time period of 30 s. This was an important milestone in investigating the use of resistive pulsed low-field magnets for hyperpolarized gas imaging.

4.7 Measurements of Diffusion Using PGSE Sequence

To determine the relaxation rate arising from the diffusion of spins through magnetic field gradients ($1/T_D$ in Eq. 4.23), we need to know the value of diffusion coefficients for the gas mixture used in our experiments. Appendix A gives a theoretical estimation of the observable diffusion coefficients of ^{129}Xe and ^{3}He in the binary gas mixture with nitrogen gas, based upon Lennard-Jones potentials. For measurements of ^{129}Xe diffusion, a cell containing 0.48 atm of naturally abundant ^{129}Xe and 0.14 atm of nitrogen was used. The theoretical calculation gave an observable diffusion coefficient for ^{129}Xe of $(1.08 \pm 0.08) \times 10^{-5}$ m^2/s. For measurements of ^{3}He diffusion, we used a cell that contained 0.75 atm of pure ^{3}He gas and 0.1 atm of nitrogen. The calculations yielded an observable diffusion coefficient for ^{3}He of $(1.77 \pm 0.12) \times 10^{-4}$ m^2/s. The diffusion coefficient of water is 2.26×10^{-9} m^2/s [84].

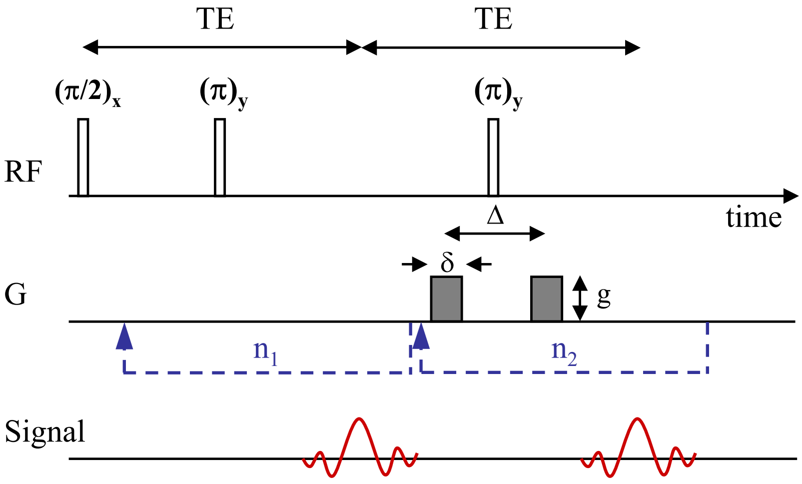

Figure 4.16: Pulse sequence used for measuring diffusion coefficients of hyperpolarized gases and water. First n_1 loops: no gradients used; last n_2 loops: bipolar gradients with amplitude = g, width = δ, separation = Δ.

The pulse sequence used for measurements of the diffusion coefficients is shown in Figure 4.16. A pair of bipolar pulsed gradients of size g, width δ, and separation Δ, was added between each acquisition to the standard CPMG sequence (Figure 4.11). Since each 180-degree pulse inverts the sign of the preceding gradients, the area under the gradient waveform is zero at the time of each acquisition. The first n_1 echoes were acquired with the gradient amplitude set to zero, while the last n_2 echoes were acquired at a fixed value of g.

As a result, there was an extra decay due to diffusion in the bipolar gradients during the last n_2 echoes only.

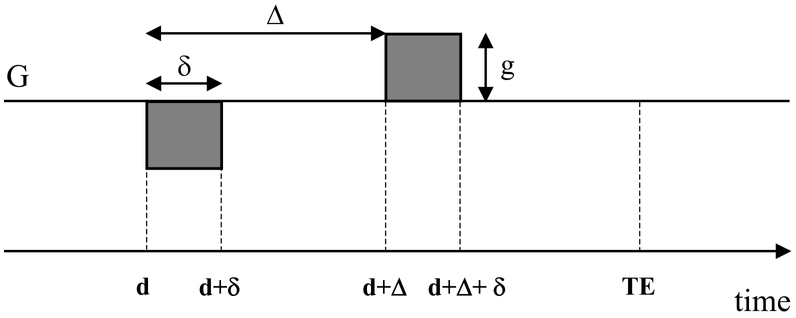

Figure 4.17: Bipolar gradient waveform used in the diffusion sequence as a function of time.

To find this decay, we refer back to the Eq. 4.41 [59],

$$A(t) = A_\circ \exp\left[-D\gamma^2 \int_0^t \left(\int_0^{t'} \mathbf{g}(t'')dt''\right)^2\right]. \tag{4.70}$$

The signal decay due to diffusion is obtained by integrating the gradient waveform over time. The bipolar gradients used in our diffusion experiments (Figure 4.16) are displayed again in Figure 4.17, this time explicitly showing the sign inversion of the first gradient lobe due to the 180-degree pulse. The time integral of $\mathbf{g}$ from the beginning of the waveform to the occurrence of the spin echo at time $t = TE$ is

$$\int_0^{t'} \mathbf{g}(t')dt'' = \begin{cases} 0 & 0 < t < d \\ -g(t'-d) & d < t < d+\delta \\ -g\delta & d+\delta < t < d+\Delta \\ -g\delta + g(t'-d-\Delta) & d+\Delta < t < d+\Delta+\delta \\ -g\delta + g\delta & d+\Delta+\delta < t < TE \end{cases} \tag{4.71}$$

and the time integral of $\mathbf{k}^2$ is

$$\begin{aligned} \int_0^t \left(\int_0^{t'} \mathbf{g}(t'')dt''\right)^2 &= -\int_d^{d+\delta} g^2(t'-d)^2 dt' - \int_{d+\delta}^{d+\Delta} g^2\delta^2 dt' \\ &\quad + \int_{d+\Delta}^{d+\Delta+\delta} \left[g^2\delta^2 - 2g^2\delta(t'-d-\Delta) + g^2(t'-d-\Delta)^2\right] dt' \end{aligned}$$

$$= g^2\delta^2\left(\Delta - \frac{\delta}{3}\right). \tag{4.72}$$

To obtain the amplitude of the nth echo we need to sum n such integrals. Thus,

$$A(nTE) = A_\circ \exp\left[-D\, n\gamma^2 g^2\delta^2\left(\Delta - \frac{\delta}{3}\right)\right], \tag{4.73}$$

where D is the diffusion coefficient of the sample, $A_\circ$ is the initial signal amplitude, and γ is the gyromagnetic ratio in radial units (i.e., rad/s/T).

We are now able to express the echo amplitude as a function of the interecho time TE during the diffusion sequence from Figure 4.16,

$$A(n_1TE) = A_\circ \exp\left(-\frac{n_1TE}{T_2^{CPMG}}\right) \tag{4.74}$$

$$A\left((n_1+n_2)TE\right) = A_\circ \exp\left(-\frac{(n_1+n_2)TE}{T_2^{CPMG}} - D\, n_2\gamma^2 g^2\delta^2\left(\Delta - \frac{\delta}{3}\right)\right). \tag{4.75}$$

Equation 4.74 refers to the echo amplitude of the first n_1 echoes (at times n_1TE), while Eq. 4.75 refers to the echo amplitude of the last n_2 echoes (at times $(n_1+n_2)TE$). By taking the logarithm of each equation above, we obtain two straight lines. A least-square-fit to the two lines produces four parameters–slope and intersect of the first line, P_1 and P_2, and slope and intersect of the second line, R_1 and R_2, where

$$\begin{aligned}
P_1 &= -\frac{1}{T_2^{CPMG}} \\
P_2 &= \ln A_\circ \\
R_1 &= -\frac{1}{T_2^{CPMG}} - D\frac{b}{TE} \\
R_2 &= Dn_1b + \ln A_\circ
\end{aligned}$$

and $b \equiv \gamma^2 g^2\delta^2(\Delta - \delta/3)$. The above equation can be rewritten in matrix form as $A\cdot x = B$, where

$$A = \begin{bmatrix} 0 & -1 & 0 \\ 1 & 0 & 0 \\ 0 & -1 & -\frac{b}{TE} \\ 1 & 0 & n_1b \end{bmatrix} B = \begin{bmatrix} P_1 \\ P_2 \\ R_1 \\ R_2 \end{bmatrix} x = \begin{bmatrix} \ln A_\circ \\ 1/T_2^{CPMG} \\ D \end{bmatrix}. \tag{4.76}$$

Since there are four parameters (vector B), but only three unknowns (vector x), the system is over-constrained [85].[13] The problem is then to search for the least-square solution $\bar{x}$ that minimizes the error $E = (B - A\bar{x})$. Geometrically, this translates to searching for a solution $\bar{x}$ such that the error vector E will be perpendicular to every column of A (or every row of A^T). Therefore,

$$\begin{aligned} A^T\left(B - A\bar{x}\right) &= 0 \\ \bar{x} &= \left(A^T A\right)^{-1} A^T b \qquad (4.77) \\ D &= \bar{x}(3). \qquad (4.78) \end{aligned}$$

We have demonstrated that by fitting the echo amplitudes obtained with the diffusion sequence to two straight lines, we can obtain an estimation of the diffusion constant using Eqs. 4.77 and 4.78.

Figures 4.18, 4.19 and 4.20 show an example of diffusion measurements for ^{3}He, ^{129}Xe and water, respectively. Figures on the left display the echo magnitude as a function of acquisition time, while figures on the right show the average echo magnitude plotted on a logarithmic scale as a function of real time and best linear fit to the data. From the log plots one can see a clear change in the slope of the two linear fits, which can be attributed to diffusion losses in bipolar gradients during the last n_2 echoes.

The difference in the slopes of the two straight fits depends on the parameter b (see Eq. 4.42). In the case of bipolar gradients of amplitude g, width δ, and separation Δ, the value of b for the n_2th echo is

$$b \equiv 4\pi^2 \int_0^t k^2(\tau)d\tau = n_2\gamma^2 g^2 \delta^2 \left(\Delta - \frac{\delta}{3}\right). \qquad (4.79)$$

In our experiments, we chose values of b that produced a visible change in the slope of the two linear fits. For ^{3}He, $b(n_2 = 1)$ ranged from 0.5×10^3 s/m^2 to 2×10^3 s/m^2, for ^{129}Xe from 4×10^3 s/m^2 to 2.5×10^4 s/m^2, and for water from 3.5×10^7 s/m^2 to 1.5×10^8 s/m^2. We observed that a value of b which was smaller than the lower limit of the intervals given above produced large uncertainties in the measurements of diffusion coefficients for xenon and helium, and gave unreasonable results (i.e., negative D values) for the diffusion

---

[13] There will not exist a choice of x that perfectly fits the parameters of B.

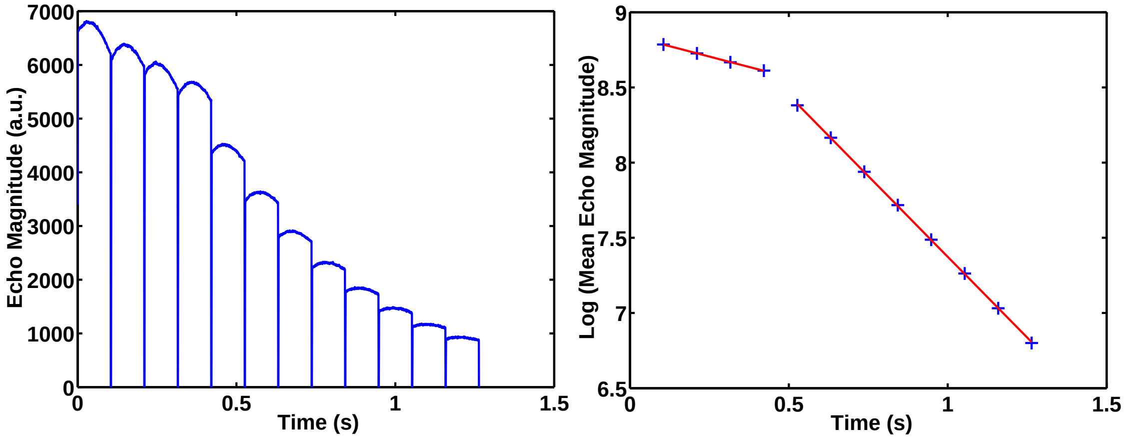

Figure 4.18: Left: ^{3}He spin echo train obtained with diffusion sequence from Figure 4.16. Right: Average echo amplitude from (right) plotted on a log scale as a function of time and best fit to data. n_1=4: g=0; n_2=8: g=0.368 mT/m; TE=105.35 ms, Δ=10.09 ms, δ=5 ms.

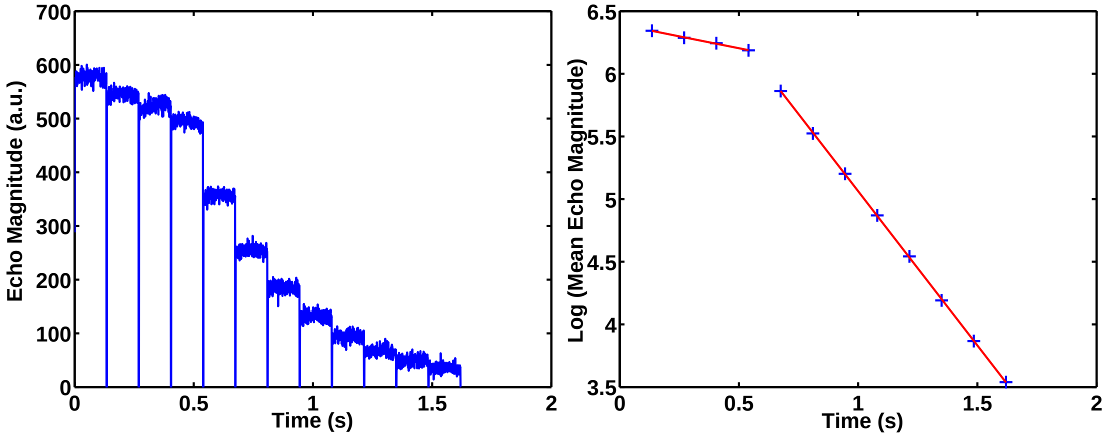

Figure 4.19: Left: ^{129}Xe spin echo train obtained with diffusion sequence from Figure 4.16. Right: Average echo amplitude from (right) plotted on a log scale as a function of time and best fit to data. n_1=4: g=0; n_2=8: g=2.76 mT/m; TE=135 ms, Δ=25.22 ms, δ=5 ms.

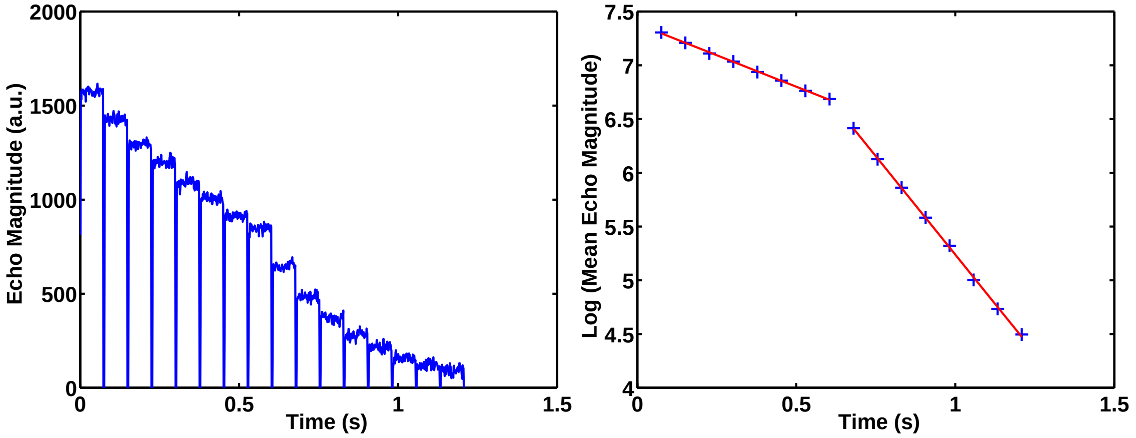

Figure 4.20: Left: Water spin echo train obtained with diffusion sequence from Figure 4.16. Right: Average echo amplitude from (right) plotted on a log scale as a function of time and best fit to data. n_1=8: g=0; n_2=8: g=13.8 mT/m; TE=75.55 ms, Δ=35.13 ms, δ=15 ms.

coefficient of water. The problem lies in the fact that a small value of b, combined with a small diffusion coefficient of water D_{H_2O}, produces a signal decay e^{-Db} which is smaller than the statistical variation of our measurements. Dividing the data into two parts and then fitting each part to a straight line can result in a negative slope difference and thus a negative diffusion coefficient.

4.7.1 Uncertainties in Determining Diffusion Coefficients of Hyperpolarized ^{129}Xe and ^{3}He

Let us first estimate the uncertainty in the theoretical estimation of diffusion coefficients for bipolar gas mixtures. Since the calculations involve many tabulated parameters, they are presented in Appendix A. From Eqs. A.2, A.4, and A.5 we see that the largest uncertainty in the estimation of observable diffusion coefficient of ^{129}Xe and ^{3}He comes from the uncertainty in the temperature of the gas inside the cell and, to a lesser extent, from the uncertainty in the pressures of the gases in the binary gas mixture. By performing simple experiments in which we measured the temperature of ^{129}Xe and ^{3}He cells during optical pumping and then again 2-5 min after cooling them in cold water, we were able to determine that the temperature of the ^{129}Xe cell was 30 ± 10°C, while the temperature of the ^{3}He cell (which was pumped at a higher temperature than ^{129}Xe) was 35 ± 10°C. The uncertainty in the pressure of gases inside the cell is directly related to the accuracy of the cell-filling process which we estimated to be ±0.01 atm.

To estimate the uncertainty in the measurement of diffusion coefficient we return to Eqs. 4.76, 4.77, and 4.78. The diffusion coefficient D is a function of the elements of matrices A and B:

$$D = \frac{TE}{b\,(1 + n_1^2\,TE^2)}\,\{P(1) - n_1\,TE\,P(2) - R(1) + n_1\,TE\,R(2)\}\,. \tag{4.80}$$

Therefore, the uncertainty in D will mainly be a function of the uncertainties in b, TE, and uncertainties in the fit parameters $P(1)$, $P(2)$, $R(1)$, $R(2)$. From Figures 4.18, 4.20 and 4.19 we can see that the fits match the data almost perfectly, so the uncertainties in the fit parameters can be ignored. The uncertainty in the interecho time should also be negligible, because the console system can generates time intervals with 10 μs accuracy, while the smallest interecho times were 5 ms. The uncertainty from the TE times would thus be less than 0.5%.

Finally, it is important to evaluate the uncertainty in the parameter $b \equiv \gamma^2\delta^2(\Delta - \delta/3)$. The dominant error in b comes from the gradient strength $g = \eta\, I$, where η is the gradient efficiency coefficient in units of mT/m/A, and I is the current through the gradient coils in units of Amperes. The gradient efficiencies were calibrated for each gradient coil with 5% accuracy. Since the gradient efficiency is the dominant source of uncertainty, we conclude that the measurements of ^{129}Xe, ^{3}He and water diffusion coefficients are $\Delta D/D = 2\Delta g/g =$ 10% accurate. This estimation is also consistent with the spread of D values obtained from repeated measurements.

	D (m^2/s) Experimental	D (m^2/s) Theory
^{129}Xe	(1.28 +/- 0.13) x 10^{-5}	(1.08+/-0.08) x 10^{-5}
^{3}He	(1.69 +/- 0.17) x 10^{-4}	(1.77 +/-0.12) x 10^{-4}
H_2O	(2.10 +/- 0.21) x 10^{-9}	(2.0 +/- 0.3) x 10^{-9}

Table 4.2: Table of experimental and theoretical values of diffusion coefficients for ^{129}Xe, ^{3}He and distilled water.

Table 4.2 summarizes the experimental values of ^{129}Xe, ^{3}He and water diffusion coefficients obtained on the pulsed low-field resistive scanner using the pulse sequence from Figure 4.16, and compares them to the theoretical values which are calculated in Appendix A. The theoretical value for the water diffusion coefficient was obtained from Piton *et.al.* [84].

4.8 Measurement of Intrinsic (Spin-Spin) T2 Relaxation Using CPMG Sequence with Variable Interecho Times

At the end of Section 4.6 we indicated that the measured T_2^{CPMG} of hyperpolarized gases depends strongly on the interecho time TE used in the CPMG sequence. We are now going to investigate this dependence in more detail.

The T_2^{CPMG} measurements showed that using longer interecho times in the CPMG sequence resulted in shorter measured T_2^{CPMG} relaxation times. This dependence is indicative of diffusion-induced losses (see Section 4.4.1) which occur when spins diffuse out of the voxel that is being inverted and refocused by the 180-degree pulse of the CPMG sequence. The longer the time between two successive 180-degree pulses (which equals the interecho time TE in Figure 4.11), the bigger the average distance travelled by the spins during that time and the bigger the loss of signal coherence. However, diffusion loss is the result of random phase accretion when spins diffuse through magnetic field gradients, and there were no external gradients used in the CPMG pulse sequence of Figure 4.11. Does this mean the reasoning just presented is flawed? Not really. Even though there were no external gradients applied during the CPMG sequence of Figure 4.11, there were gradients present due to magnetic field inhomogeneity as well as gradients due to the magnetic field susceptibility differences between air and the sample.[14] These gradients, which are constant throughout the CPMG sequence, are estimated to be small (on the order of 0.1 mT/m), yet can cause a detectable signal loss because of the large diffusion constant of gases.

To compute signal decay due to constant gradients we refer back to Figure 4.17 and Eq. 4.73. The amplitude of the nth echo in the case of constant gradients is the limiting case of Eq. 4.73, with $\delta \to TE/2$ and $\Delta \to \delta$. At time $t = nTE$,

$$\begin{aligned} A(nTE) &= \lim_{\delta=\Delta\to TE/2} \left\{ A_\circ \exp\left[-D\, n\gamma^2 g^2 \delta^2 \left(\Delta - \frac{\delta}{3}\right)\right]\right\} \\ &= A_\circ \exp\left[-\frac{1}{12}\, Dn\gamma^2 g^2 TE^3\right]. \end{aligned} \tag{4.81}$$

---

[14] In the case of spherical glass cells, the susceptibility effects are negligible.

By adding the decay due to the inherent $T2$ relaxation, we get

$$A(nTE) = A_\circ \exp\left(-\frac{nTE}{T_2}\right) \exp\left(-\frac{1}{12}\, Dn\gamma^2 g^2 TE^3\right). \tag{4.82}$$

Since the detected relaxation rate is $1/T_2^{CPMG}$, the two exponentials can be combined into a single decay term,

$$\begin{aligned} A(nTE) &= A_\circ \exp\left(-\frac{nTE}{T_2^{CPMG}}\right), \text{ where} \\ \frac{1}{T_2^{CPMG}} &\equiv \frac{1}{T_2} + \frac{1}{12} D\gamma^2 g^2 TE^2. \end{aligned} \tag{4.83}$$

The above equation expresses the relationship between the T_2^{CPMG} relaxation time and the interecho time TE. We see that the inherent T_2 relaxation is equal to T_2^{CPMG} relaxation at $TE = 0$.

We performed T_2^{CPMG} measurements using the pulse sequence shown in Figure 4.11 and with TE times ranging from 5 ms to above 100 ms for ^{129}Xe, ^{3}He and water. We then plotted T_2^{CPMG} versus TE and fitted the data using least-square method to a two-parameter function of the form

$$F(TE) = \frac{1}{1/a + bTE^2}. \tag{4.84}$$

Using Eq. 4.83, the values of a and b give the inherent T_2 relaxation and the gradient amplitude due to the magnetic field inhomogeneities, respectively:

$$T_2 = a \tag{4.85}$$

$$g = \sqrt{\frac{12b}{D\gamma^2}}\,. \tag{4.86}$$

Since the inherent T_2 relaxation and the gradient amplitude g are independent of each other, we should obtain, within the experimental error, same T_2 relaxation times regardless of the size of the background gradients. We therefore repeated the $T_2^{CPMG}(TE)$ measurements for a range of g values (0.01 mT/m-0.4 mT/m) which were controlled with the size of the shimming currents applied to the magnetic field gradients (see beginning of Section 4.5). The measurements of T_2^{CPMG} for different g values should, in theory, converge to a single point at $TE = 0$.

Figures 4.21, 4.22, and 4.23 show the results of our $T_2^{CPMG}(TE)$ measurements for ^{3}He, ^{129}Xe, and water, respectively. Water measurements were done on distilled water as well as water doped with 0.012 molar $CuSO_4 \cdot 5H_2O$–a substance which decreases the T_2 relaxation time of water. Only the results for the distilled water are shown. The water measurements should show no variation in the measured T_2^{CPMG} beyond the statistical error because of the small diffusion constant of water (see Section 4.7). This is confirmed in Figure 4.23. The average T_2 relaxation time of distilled water was 1 s, while T_2 of doped water was around 42 ms. Both results are in agreement with expectations.

Analysis of the three sets of ^{129}Xe T_2^{CPMG} data in Figure 4.22 results in an inherent T_2 relaxation of ^{129}Xe equal to 46.7 ± 0.5 s. On the other hand, the inherent T_2 relaxation time of ^{3}He for the two sets of data in Figure 4.21 is equal to 19.2 ± 4.5 s. In the next section we examine the sources of errors involved in obtaining this data.

4.8.1 Uncertainties in Determining Inherent T2 Relaxation of Hyperpolarized ^{129}Xe and ^{3}He

Equation 4.84 tells us that the inherent T_2 relaxation of ^{129}Xe and ^{3}He is obtained from one of the parameters of a two-parameter fit. The quality of the fit will thus determine the uncertainty in the inherent T_2 time. In addition, we need to examine the uncertainty associated with the data of Figures 4.21 and 4.22. Each data point in these plots was obtained from the least-square fit of the CPMG echo train (see Figure 4.13). Consequently, the uncertainty in the extracted T_2^{CMPG} time constant will contribute to the uncertainty in the data points of Figures 4.21 and 4.22. By shifting the data in the vicinity of $TE = 0$ for the amount of T_2^{CPMG} uncertainty we concluded that the uncertainty in the estimation of the inherent T_2 is between 3% and 6%.

The uncertainty of 6% is sufficient to explain the variation in the extrapolated T_2 times for the three sets of ^{129}Xe data, but it does not suffice to explain the 20% error in the ^{3}He data. We thus have to look at possible systematic errors.

There are many effects which can shorten the measured T_2^{CPMG} times. We mentioned some of them, such as the uncertainties in the calibration of the 180-degree pulses and the off-resonance effect due to the resistive heating of the magnet, in Sections 4.6.1 and 4.6.2. However, none of these possible sources of error should affect ^{3}He data more than ^{129}Xe. One major difference between ^{3}He and ^{129}Xe experiments was the temperature of the cell

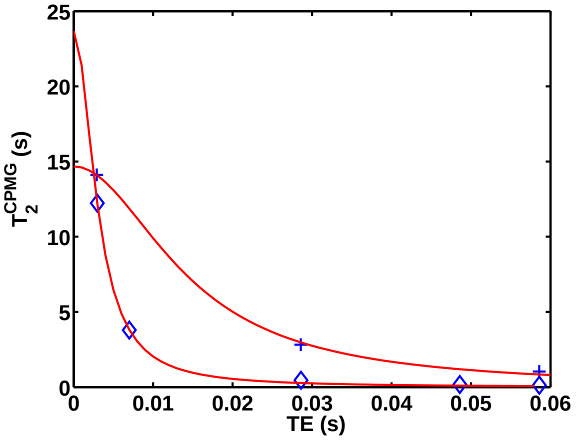

Figure 4.21: ^{3}He T_2^{CPMG} data as a function of interecho time, TE, for two shimming values, and a fit to the data according to Eq 4.84. $g \approx 0.06$ mT/m, $T_2 = 23.7$ s; $g \approx 0.01$ mT/m, $T_2 = 14.7$ s.

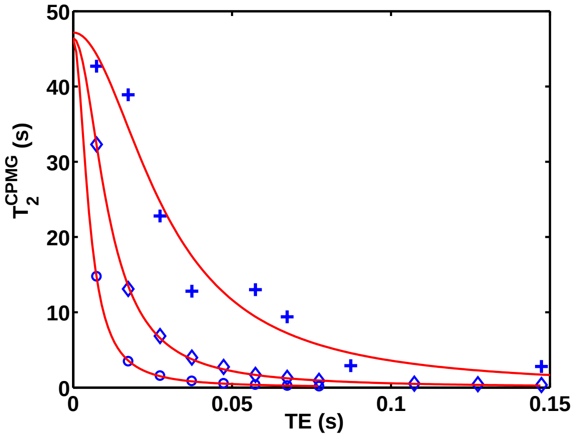

Figure 4.22: ^{129}Xe T_2^{CPMG} data as a function of interecho time, TE, for three shimming values, and a fit to the data according to Eq 4.84. $g \approx 0.02$ mT/m, $T_2 = 47.2$ s; $g \approx 0.13$ mT/m, $T_2 = 46.5$ s; $g \approx 0.38$ mT/m, $T_2 = 46.3$ s.

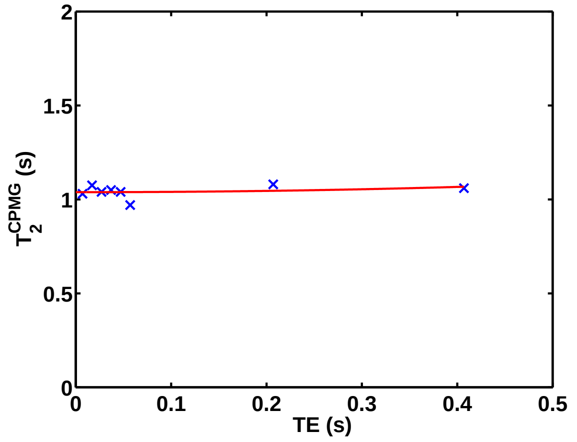

Figure 4.23: Distilled water T_2^{CPMG} data as a function of interecho time, TE, and a fit to the data according to Eq 4.84. $g = 0.005$ mT/m, $T_2 = 1.04$ s.

during optical pumping (120°C for ^{3}He vs. 80°C for ^{129}Xe). Since the signals were collected immediately after placing the cell into the low-field scanner for best SNR values, the ^{3}He cell might not have been in thermal equilibrium during data acquisition and the gas inside the cell might have been undergoing convective flow.

To understand how flow of gas inside the cell would decrease the echo magnitude and contribute to T_2^{CPMG} decay, we return to Eq. 4.40. The second term on the right hand side represents the phase shift of the echo in the presence of flow with velocity $\mathbf{v}$. Since no external gradients were applied during the CPMG sequence, the gradient $\mathbf{g}(t)$ in Eq. 4.40 will be due to the magnetic field inhomogeneities. For a constant background inhomogeneity of magnitude g, the time integral reduces to

$$\int_0^t \left(\int_0^{t'} g(t'')dt'' \right) dt' = -\frac{1}{4}\, g\, TE^2. \tag{4.87}$$

The second term in Eq. 4.40 thus becomes

$$\exp\left[i\gamma \mathbf{v} \cdot \int_0^t \left(\int_0^{t'} \mathbf{g}(\tau)d\tau \right) dt' \right] = \exp\left[-\frac{i}{4}\, \gamma\, \mathbf{v} \cdot \mathbf{g}\, TE^2 \right] \tag{4.88}$$

For ^{3}He, $\gamma = 32.43$ kHz/mT, g was on the order of 0.1 mT/m, and the shortest TE time was 7 ms.[15] In the worst-case scenario, $\mathbf{v} \cdot \mathbf{g} = v\, g$. For a 1-degree phase shift we have

$$\begin{aligned} \exp\left[-\frac{1}{4}\, \gamma\, v\, g\, TE^2 \right] &= \exp\left[-i \frac{\pi}{180} \right] \\ v &= 1 \text{ cm/s}. \end{aligned} \tag{4.89}$$

The result tells us that if the convective flow moves with velocity of 1 cm/s (a plausible assumption), each spin echo would be phase-shifted 1-degree from the previous one. This would violate the CPMG condition which requires that the axis of rotation remains parallel to the gas magnetization (see also Section 4.6.2) and result in an accelerated decay of spin echoes and a shorter T_2^{CPMG} time.

We tested our "flow" hypothesis by performing some simple tests. Table 4.3 gives an overview of these tests and the corresponding qualitative results. On the basis of the test results we were able to form the following conclusions: 1. Shaking the cell and so disturbing

---

[15] The error in T_2^{CPMG} of the echo train with the shortest TE time will weight the most in the evaluation of the error in T_2.

the gas inside the cell does indeed affect the quality of spin echoes and the rate of decay of the spin echo train; 2. In our *in vitro* experiments the effect of gas movement (due to shaking or high temperatures) subsides after 10-20 s, hence data acquisition should not begin before the gas had the time to reach thermal equilibrium; 3. Spin echoes decay faster if the cell is not at room temperature during data acquisition, although more studies (possibly with ^{3}He gas rather than ^{129}Xe) would have to be done to understand whether this effect is due to hyperpolarized gas relaxation resulting from collisions with unpolarized Rb vapor or due to the effects of gas flow.

In summary, we think that either shaking of the cell and/or not cooling the gas inside the cell to room temperature affected our T_2^{CPMG} data and thus contributed to the error in the inherent ^{3}He T_2 relaxation times. Evaluating the size of this systematic error would require a more detailed study. Alternatively, we could increase the statistics of ^{3}He data.

Finally, understanding the effects of flow on a CPMG spin echo train and the measured T_2^{CPMG} relaxation time would be essential in *in vivo* experiments, due to the motion (flow) of gas through the bronchi and lungs.

Flow Tests using Xe cell	Qualitative Results	
	Quality of Spin-Echo Train	Rate of Spin-Echo Decay
Shaking the cell vigorously before data acquisition	Poor	Fast
No shaking before data acquisition	Good	Slow
Shaking + waiting 10 sec before data acquisition	Good	Slow
No cooling of the cell before data acquisition	Bad	Fast
Cooling for 10 sec before data acquisition	Good	Fast
Cooling for 20 sec before data acquisition	Good	Slow

Table 4.3: Results of simple qualitative experiments testing the hypothesis of gas flow.

4.9 Conclusions

We have investigated the possibility of using a pulsed (or variable) rather than a static resistive system for low-field hyperpolarized gas imaging. In particular, the field instability at 397 kHz (i.e., 33 mT for ^{129}Xe) is small enough to allow the implementation of the CPMG spin echo sequence. We were able to collect ^{129}Xe CPMG spin echo trains lasting over 30 s and following a well behaved exponential decay. In addition, by adding a small offset field to the readout magnet, we guaranteed an adiabatic transition in magnetization alignment during the pulsing of the readout magnet and hence prevented loss of gas polarization.

We have developed a single-shot sequence for measuring diffusion coefficients of gases which separates diffusion losses from T_2^{CPMG} relaxation losses. Our diffusion sequence was a variation of the pulsed gradient spin echo sequence, with external gradients applied in the second half of the sequence only. For the binary mixture of hyperpolarized gas and nitrogen, the experimental values of ^{3}He, ^{129}Xe and water diffusion coefficients were: $D_{He3} = (1.69 \pm 0.17) \times 10^{-4}$ m^2/s, $D_{Xe129} = (1.28 \pm 0.13) \times 10^{-5}$ m^2/s, and $D_{H_2O} = (2.10 \pm 0.21) \times 10^{-9}$ m^2/s. The dominant experimental error was due to the uncertainty in the gradient strengths. This error could easily be reduced in the future by calibrating the gradient strengths more accurately. Finally, the experimental measurements agree well with the theoretical calculations of diffusion coefficients using Lennard-Jones [30] potentials.

Because diffusion coefficient is dependent on the cell pressure and gas composition, it is difficult to compare our data with the existing experimental data on diffusion coefficients. Schmidth *et al.* [80] measured a ^{3}He diffusion coefficient of 21.3 ± 0.4 mm^2/s at 7 atm of gas, which translates to $(1.491 \pm 0.028) \times 10^{-4}$ m^2/s at 1 atm of gas and agrees well with our measurement to within the uncertainty in the nitrogen pressure used in their experiment. Peled *et al.* [82] measured a ^{129}Xe diffusion coefficient of 0.0579×10^{-4} m^2/s, which is very close to our calculated ^{129}Xe self-diffusion coefficient (see Appendix A), so we conclude that their gas mixture had negligible amounts of nitrogen gas.

Finally, by varying the interecho time in the CPMG sequence we were able to determine the T_2 relaxation time at zero interecho spacing, which represents the inherent T_2 decay of hyperpolarized gas and is the upper limit on the time available for spin echo imaging. We measured an inherent ^{129}Xe T_2 relaxation of 46.7 ± 0.5 s, and an inherent ^{3}He T_2 relaxation of 19.2 ± 4.5 s. We hypothesize that the large error in the ^{3}He data might be due to the flow (motion) of gas inside the cell, which would result if the cell is not in thermal equilibrium during data acquisition or is shaken before being placed in the scanner.

Most of the T_2 values quoted in literature are the T_2^{CPMG} times which include diffusion losses in the background gradients. For instance, Pfeffer *et al.* [86] point out that their T_2 measurement was influenced by the field inhomogeneities so that the ^{129}Xe relaxation time of 12.9 ± 1.9 s was the lower limit on ^{129}Xe T_2 relaxation. Darrasse *et al.* [47] measured T_2^{CPMG} for ^{3}He in lungs at two different interecho times (10 ms, 30 ms) but did not use their measurements to find the inherent T_2 in lungs.

For future work, it would be interesting to see whether our method for determining the inherent T_2 times would be applicable to *in vivo* experiments. When imaging lungs, the effect of gas flow on the T_2 measurements would need to be studied in detail. However, such a study requires a full body scanner.